Cancer Cell

Article

Spatial determinants of antibody-drug conjugate SHR-A1811 efficacy in neoadjuvant treatment for HER2-positive breast cancer

Graphical abstract

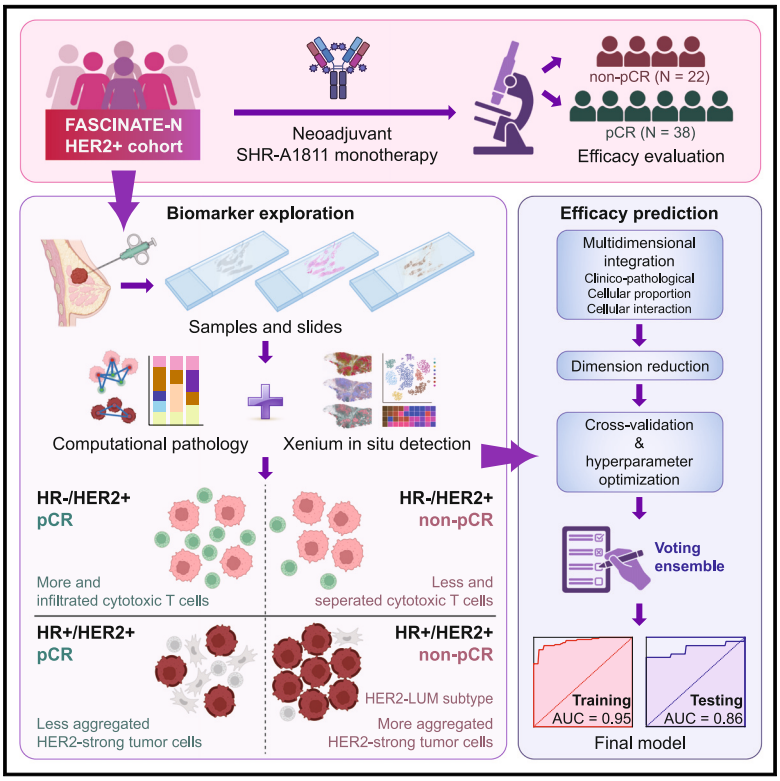

Highlights

- Spatially derived biomarkers inform response to neoadjuvant anti-HER2 ADC treatment
- More infiltrated TILs (cytotoxic T cells) correlated with pCR in HR− breast cancer
- Aggregated HER2-strong-positive tumor cells correlated with non-pCR in HR+ breast cancer
- AI-model predicted benefit to neoadjuvant next-generation ADC in HER2+ breast cancer

Authors

Ding Ma, Lei-Jie Dai, Xiang-Rong Wu, ..., Wen-Tao Yang, Yi-Zhou Jiang, Zhi-Ming Shao

Correspondence

lijunjie_ronaldo@hotmail.com (J.-J.L.), yangwt2000@163.com (W.-T.Y.), yizhoujiang@fudan.edu.cn (Y.-Z.J.), zhimingshao@fudan.edu.cn (Z.-M.S.)

In brief

Ma et al. conduct a translational study on HER2+ breast cancer receiving neoadjuvant SHR-A1811. They identify immune cell infiltration and HER2-strong-positive tumor cell distribution as response biomarkers in HR− and HR+ subgroups, respectively. Additionally, they developed a model leveraging clinicopathological features and routine pathology slide images to forecast treatment response.

Ma et al., 2025, Cancer Cell *43*, 1–15
June 9, 2025
https://doi.org/10.1016/j.ccell.2025.03.017

CellPress

Cancer Cell

CellPress

Article

Spatial determinants of antibody-drug conjugate SHR-A1811 efficacy in neoadjuvant treatment for HER2-positive breast cancer

Ding Ma,[1,2,8] Lei-Jie Dai,[1,2,8] Xiang-Rong Wu,[1,2,8] Cheng-Lin Liu,[1,2,8] Shen Zhao,[1,2] Hang Zhang,[1,2] Li Chen,[1,2] Yi Xiao,[1,2] Ming Li,[2,3] Yi-Zhi Zhao,[5,6] Lin Yang,[5,6] Tong Zhou,[7] Jun-Jie Li,[1,2,*] Wen-Tao Yang,[2,3,*] Yi-Zhou Jiang,[1,2,4,*] and Zhi-Ming Shao[1,2,9,*]

[1]Department of Breast Surgery, Key Laboratory of Breast Cancer in Shanghai, Fudan University Shanghai Cancer Center, Shanghai 200032, China
[2]Department of Oncology, Shanghai Medical College, Fudan University, Shanghai 200032, China
[3]Department of Pathology, Fudan University Shanghai Cancer Center, Shanghai 200032, China
[4]Shanghai Academy of Natural Sciences (SANS), Fudan University, Shanghai 200030, China
[5]School of Engineering, Westlake University, Hangzhou 310030, China
[6]Hangzhou DiPath Technology Co. Ltd., Hangzhou 311121, China
[7]Shanghai Institute of Preventive Medicine, Shanghai 201416, China
[8]These authors contributed equally
[9]Lead contact
*Correspondence: lijunjie_ronaldo@hotmail.com (J.-J.L.), yangwt2000@163.com (W.-T.Y.), yizhoujiang@fudan.edu.cn (Y.-Z.J.), zhimingshao@fudan.edu.cn (Z.-M.S.)
https://doi.org/10.1016/j.ccell.2025.03.017

SUMMARY

Selecting optimal candidates for next-generation anti-human epidermal growth factor receptor 2 (HER2) antibody-drug conjugates (ADCs) remains challenging. We conduct a prespecified translational study to identify treatment biomarkers in SHR-A1811-treated HER2-positive breast cancer patients from the phase 2 neoadjuvant FASCINATE-N trial using DNA and RNA sequencing, computational pathology, and single-cell *in situ* spatial imaging. In the hormone receptor (HR)-negative subgroup, a higher proportion and more infiltration of immune cells (i.e., tumor-infiltrating lymphocytes [TILs]), particularly cytotoxic T cells, are associated with better treatment responses. In the HR-positive subgroup, the closeness and aggregation of HER2-strong-positive tumor cells, as opposed to a uniform distribution, are linked to a lower response rate and HER2 luminal-like (HER2-LUM) subtype, which more closely resembles HR+/HER2− breast cancer. In addition, we develop a clinically practical predictive model capable of predicting neoadjuvant treatment responses to SHR-A1811 and other novel ADCs based on clinicopathological characteristics and pathological images.

INTRODUCTION

Breast cancer is the most commonly diagnosed cancer and a leading cause of cancer-related mortality among women worldwide.[1] Human epidermal growth factor receptor 2-positive (HER2+) breast cancer, accounting for approximately 15%–20% of all breast cancer cases, is characterized by the overexpression of the HER2 protein and is associated with aggressive tumor behavior and poor prognosis.[2] In recent years, advances in HER2-targeted therapies, such as monoclonal antibodies, tyrosine kinase inhibitors, and antibody-drug conjugates (ADCs), have significantly improved the outcomes of patients with such conditions, transforming it to a more manageable subtype.[3] More recently, the administration of a new generation of ADCs, with linker optimization and payload selection, further enhanced their targeting specificity and therapeutic efficacy.[4,5] The rapid evolution and innovative potential of ADCs underscore their pivotal role in the future of HER2+ breast cancer treatment.

Clinical trials have demonstrated the efficacy of novel ADCs, exemplified by T-DXd, which has shown significant results across HER2+, HER2-low, and HER2-ultra-low tumors.[5–7] However, a significant number of patients still do not benefit from this treatment, and the potential for "over-application" of these ADCs raises concerns about inappropriate use, which may increase the occurrence of severe side effects, such as debilitating lung toxicity. Therefore, there is an urgent need for efficacy-related biomarkers and predictive tools to guide the precise application of these novel ADCs.

To address the challenge of precisely utilizing novel anti-HER2 ADCs in HER2+ breast cancer therapy, we conducted a translational study based on the HER2+ breast cancer cohort of our phase 2 FASCINATE-N trial (NCT05582499).[8] The FASCINATE-N trial established a platform for optimizing neoadjuvant treatment

Please cite this article in press as: Ma et al., Spatial determinants of antibody-drug conjugate SHR-A1811 efficacy in neoadjuvant treatment for HER2-positive breast cancer, Cancer Cell (2025), https://doi.org/10.1016/j.ccell.2025.03.017

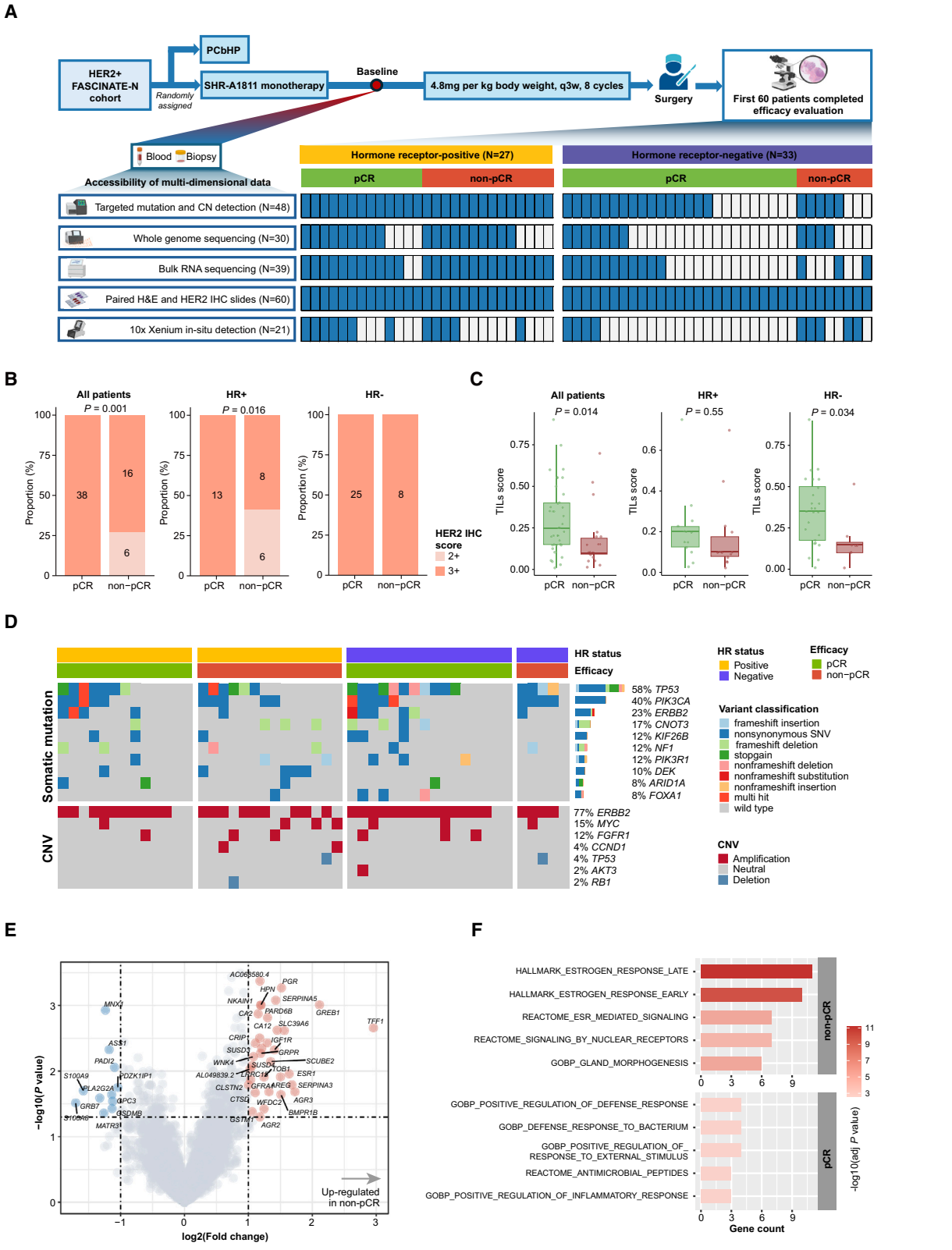

(legend on next page)

Please cite this article in press as: Ma et al., Spatial determinants of antibody-drug conjugate SHR-A1811 efficacy in neoadjuvant treatment for HER2-positive breast cancer, Cancer Cell (2025), https://doi.org/10.1016/j.ccell.2025.03.017

regimens and provided long-term, stable support for translational research derived from clinical trials. The HER2+ breast cancer cohort of the FASCINATE-N trial included patients who were randomly assigned to receive the neoadjuvant SHR-A1811 regimen for 8 cycles, compared to the standard PCbHP regimen for 6 cycles. SHR-A1811 comprises trastuzumab conjugated to a novel topoisomerase I inhibitor payload, SHR9265, via a degradable linker, with a drug-to-antibody ratio (DAR) of 5.7. Notably, SHR-A1811 has shown promising efficacy against HER2-expressing breast cancer in a recent study, with objective responses of 76.3% in advanced HER2+ breast cancer and 60.4% in HER2 low-expression breast cancer, making it an ideal regimen for studying novel anti-HER2 ADCs.[9,10]

In this study, we aimed to investigate the distinct patient characteristics associated with sensitivity to neoadjuvant SHR-A1811 treatment, with the goal of guiding the precise clinical application of this novel anti-HER2 ADC. To achieve this goal, we integrated clinical and biological evidence, leveraging bulk sequencing data, computational pathology processed with our published algorithm,[11] and *in situ* spatial imaging techniques. Using these insights, we developed a clinically practical and interpretable artificial intelligence (AI)-based prediction model for the efficacy of SHR-A1811, which can also be extrapolated to other novel HER2-targeted ADCs. By leveraging such structured and comprehensive research frameworks, we aimed to enhance personalized treatment strategies for SHR-A1811, providing precise treatment guidance for patients with HER2+ breast cancer.

RESULTS

HER2+ FASCINATE-N treatment arms and omics dimensions

Patients in the HER2+ FASCINATE-N cohort were enrolled beginning of December 27, 2022. All participants were adults with HER2+ breast cancer, defined with immunohistochemistry (IHC) score 3+ or 2+ with *in situ* hybridization amplification. The cohort included patients with early-stage disease (T2-3, N0-1, and M0) and locally advanced disease (T2-3, N2-3, M0 or T4, any N, M0). These patients were treatment-naïve, had an Eastern Cooperative Oncology Group (ECOG) performance status of 0/1. The primary endpoint of this study was pathological complete response (pCR), defined as ypT0/Tis and ypN0 after neoadjuvant therapy, as assessed by pathologists. Detailed analysis plans are outlined in the study protocol, and the trial is registered on ClinicalTrials.gov (NCT05582499).[8] According to the Bayesian design of this clinical trial, a pre-planned translational study of biomarkers was triggered upon the completion of all the neoadjuvant therapy cycles and post-surgical efficacy assessments for the first 60 patients (Figure 1A, STAR Methods).

Our study comprehensively explored multiple omics dimensions using baseline samples if they were adequate, with a specific focus on innovative spatial analysis techniques (Figure 1A). In the genomic dimension, targeted sequencing was performed on 48 patients, 30 of whom also underwent whole-genome sequencing (WGS). For transcriptomics, bulk RNA sequencing (RNA-seq) was conducted on 39 patients. We also incorporated spatial analysis. First, we conducted computational pathology on both hematoxylin and eosin (H&E)-stained and HER2 IHC-stained whole-slide images (WSIs) from all 60 patients. Additionally, we applied the Xenium *in situ* assay in 21 cases.

Clinicopathological and molecular variables are associated with the efficacy of SHR-A1811

In the monotherapy SHR-A1811 treatment arm, the efficacy results demonstrated pCR in 38 patients, yielding a pCR rate of 63.3% (Table 1). In the analysis of clinical and pathological data, we revealed that the non-pCR group exhibited higher clinical N stages ($p = 0.002$), a greater incidence of hormone receptor (HR)+ ($p = 0.034$) and progesterone receptor-positive (PR+) ($p = 0.007$) diseases, lower HER2 IHC scores ($p = 0.001$, Figure 1B) and less tumor-infiltrating lymphocytes (TILs) ($p = 0.014$, Figure 1C) compared to the pCR group. When stratified by HR status, HR+ patients achieved a pCR rate of 48.1% (13/27), while HR− patients exhibited a higher pCR rate of 75.8% (25/33) (Table S1). Specifically, among HR+ patients, non-pCR cases were associated with higher clinical N stages ($p = 0.002$), higher PR percentage ($p = 0.011$) diseases, and lower HER2 IHC scores ($p = 0.016$, Figure 1B) compared to pCR cases. In contrast, within the HR− subgroup, non-pCR tumors showed significantly less TILs compared to pCR cases ($p = 0.034$, Figure 1C).

Regarding genomic features, neither somatic mutations nor copy number variations (CNVs) were significantly different between the pCR and non-pCR group in the entire cohort or in either HR subgroup (Figures 1D; Tables S2 and S3), which was also confirmed by WGS data (Figure S1A).

Then we investigated the difference in transcriptional level. Direct comparison between pCR and non-pCR tumors revealed upregulation of immune-related genes in pCR tumors, and estrogen-related genes in non-pCR tumors (Figure 1E), which was

Figure 1. Cohort information, clinicopathological features, and genomic characteristics

(A) Treatment efficacy and multiomics profiling information of the HER2+ FASCINATE-N SHR-A1811 arm.

(B) Comparison of HER2 IHC score between the pCR and non-pCR group, stratified and not stratified by hormone receptor (HR) status. Statistical significance was determined using the Fisher's exact test. HER2 IHC scores were evaluated according to ASCO/CAP guidelines (STAR Methods). The numbers in the bars represent the number of samples/patients.

(C) Comparison of TILs abundance between the pCR ($n = 38$) and non-pCR ($n = 22$) group, stratified and not stratified by HR status. Statistical significance was determined using the Wilcoxon test. In boxplots, the centerline represents the median, the box limits represent the upper and lower quartiles, the whiskers represent the 1.5× interquartile range, and the points represent individual samples.

(D) Frequency of somatic mutation and copy number variation (CNV) in patients stratified by HR status and treatment response.

(E) Differentially expressed genes (DEGs) between pCR ($n = 22$) and non-pCR ($n = 17$) tumors. Red dots and blue dots represent the DEGs upregulated in non-pCR or pCR tumors, respectively. p values were derived from differential analysis with limma.

(F) Significantly enriched gene sets of DEGs in Figure 1E. Adjusted p values were derived from enrichment analysis with clusterProfiler. See also Figure S1 and Tables S1–S3.

Please cite this article in press as: Ma et al., Spatial determinants of antibody-drug conjugate SHR-A1811 efficacy in neoadjuvant treatment for HER2-positive breast cancer, Cancer Cell (2025), https://doi.org/10.1016/j.ccell.2025.03.017

Table 1. Comparison of baseline clinicopathological characteristics between patients with different efficacy

	non-pCR N = 22	pCR N = 38	p value
Age at diagnosis (mean [SD])	46.09 (10.36)	48.89 (9.69)	0.297
cT (%)			
≤2	14 (63.6)	28 (73.7)	1
3	3 (13.6)	3 (7.9)	
4	5 (22.7)	7 (18.4)	
cN (%)			
0	1 (4.5)	4 (10.5)	0.002
1	2 (9.1)	17 (44.7)	
2	6 (27.3)	11 (28.9)	
3	13 (59.1)	6 (15.8)	
HR status (%)			
Negative	8 (36.4)	25 (65.8)	0.034
Positive	14 (63.6)	13 (34.2)	
ER status (%)			
Negative	8 (36.4)	25 (65.8)	0.034
Positive	14 (63.6)	13 (34.2)	
PR status (%)			
Negative	11 (50.0)	32 (84.2)	0.007
Positive	11 (50.0)	6 (15.8)	
ER percent (mean [SD])	48.05 (42.23)	17.03 (33.87)	0.003
PR percent (mean [SD])	28.23 (35.13)	4.13 (15.36)	0.001
HER2 IHC score (%)			
2	6 (27.3)	0 (0.0)	0.001
3	16 (72.7)	38 (100.0)	
HER2 FISH (%)			
Positive	22 (100.0)	33 (100.0)	/
NA	0	5	
TILs (mean [SD])	0.17 (0.17)	0.30 (0.21)	0.014

Statistical tests of continuous variables were performed using the Wilcoxon test. Statistical tests of categorical variables were performed using Fisher's exact test or the chi-square test, where appropriate. Not available (NA) values for categorical variables were shown but were not included in the statistical analysis. SD, standard deviation; HR, hormone receptor; IHC, immunohistochemistry; FISH, fluorescence *in situ* hybridization; TILs, tumor-infiltrating lymphocytes.
See also Figure S1 and Tables S1–S3.

further supported by gene set enrichment analysis (GSEA) (Figure 1F). Then, considering the significant difference in efficacy-related clinicopathological features between tumors of different HR statuses, we performed differential analysis in each HR subgroup. In HR+ tumors, non-pCR samples consistently exhibited higher expression of estrogen-related genes, such as *PGR* and *GREB1*. GSEA underscored the role of the estrogen pathway, with "hallmark estrogen response early" and "hallmark estrogen response late" being the most enriched gene sets (Figures S1B and S1C). In the HR− subgroup, the limited sample size of non-pCR patients resulted in fewer differentially expressed genes (DEGs) and less significantly enriched gene sets (Figures S1D and S1E).

Overall, notable differences in pCR rates and efficacy-associated variables exist between the HR+ and HR− groups, emphasizing the need for HR stratification in further investigations of biomarkers. These findings suggest that patients with different HR statuses may exhibit distinct response mechanisms to SHR-A1811.

Computational pathology and Xenium depicted spatial characteristics

The spatial organization of tumors has been implicated in the treatment response to novel anti-HER2 ADCs.[12] To systemically investigate the spatial characteristics associated with the efficacy of SHR-A1811, we integrated computational pathology based on morphological features with a high-throughput *in situ* imaging array.

For computational pathology, we scanned paired pretreatment H&E-stained and HER2 IHC-stained slides to obtain high-resolution digital WSIs from all 60 patients in our cohort (Figure 2A). These images were subjected to cellular identification and topological interaction analysis using our established artificial intelligence deep learning pipeline.[11,13] This approach provides a cost-effective and generalizable method for comprehensively understanding the spatial features of HER2+ breast cancer.

Through computational pathology, we extracted multiple spatial features, as summarized in Figure 2B and Table S4. Specifically, the analysis of H&E-stained WSIs identified three cell types: tumor cells, immune cells, and stromal cells. We quantified their spatial localization, proportions among all cells, and topological interactions. In addition, we validated in two independent cohorts[14,15] that tumor microenvironment (TME) features derived from H&E-stained WSIs showed significant relation with TME cell abundance inferred from RNA-seq deconvolution (Figure S2), proving the robustness of our algorithm. In contrast, the analysis of HER2 IHC WSIs focused on tumor cells and discriminated among different HER2 staining intensities (strong-positive, weak-positive, and null), revealing their spatial relationships.

Interestingly, our findings differed significantly based on the HR status of the studied tumors (Figure 2B). In HR− patients, the analysis of H&E-stained WSIs highlighted the proportion of immune cells, spatial topological interactions between tumor and immune cells, as well as stromal cells. Conversely, in HR+ patients, significant findings were predominantly observed in the analysis of HER2 IHC-stained WSIs, specifically regarding the spatial interactions among HER2-strong-positive, HER2-weak-positive, and HER2-null tumor cells. These distinct microenvironments suggested that topological interaction patterns may influence SHR-A1811 efficacy, with cells in the TME playing a primary role in HR− patients and tumor cells themselves in HR+ patients. Additionally, we conducted similar analyses in the PCbHP group, yielding results distinct from those in the SHR-A1811 group, suggesting that the observed findings are specific to SHR-A1811 treatment (Figure S3).

We further utilized *in situ* expression arrays to obtain deeper insights into the spatial parameters.[16] We selected regions of

Please cite this article in press as: Ma et al., Spatial determinants of antibody-drug conjugate SHR-A1811 efficacy in neoadjuvant treatment for HER2-positive breast cancer, Cancer Cell (2025), https://doi.org/10.1016/j.ccell.2025.03.017

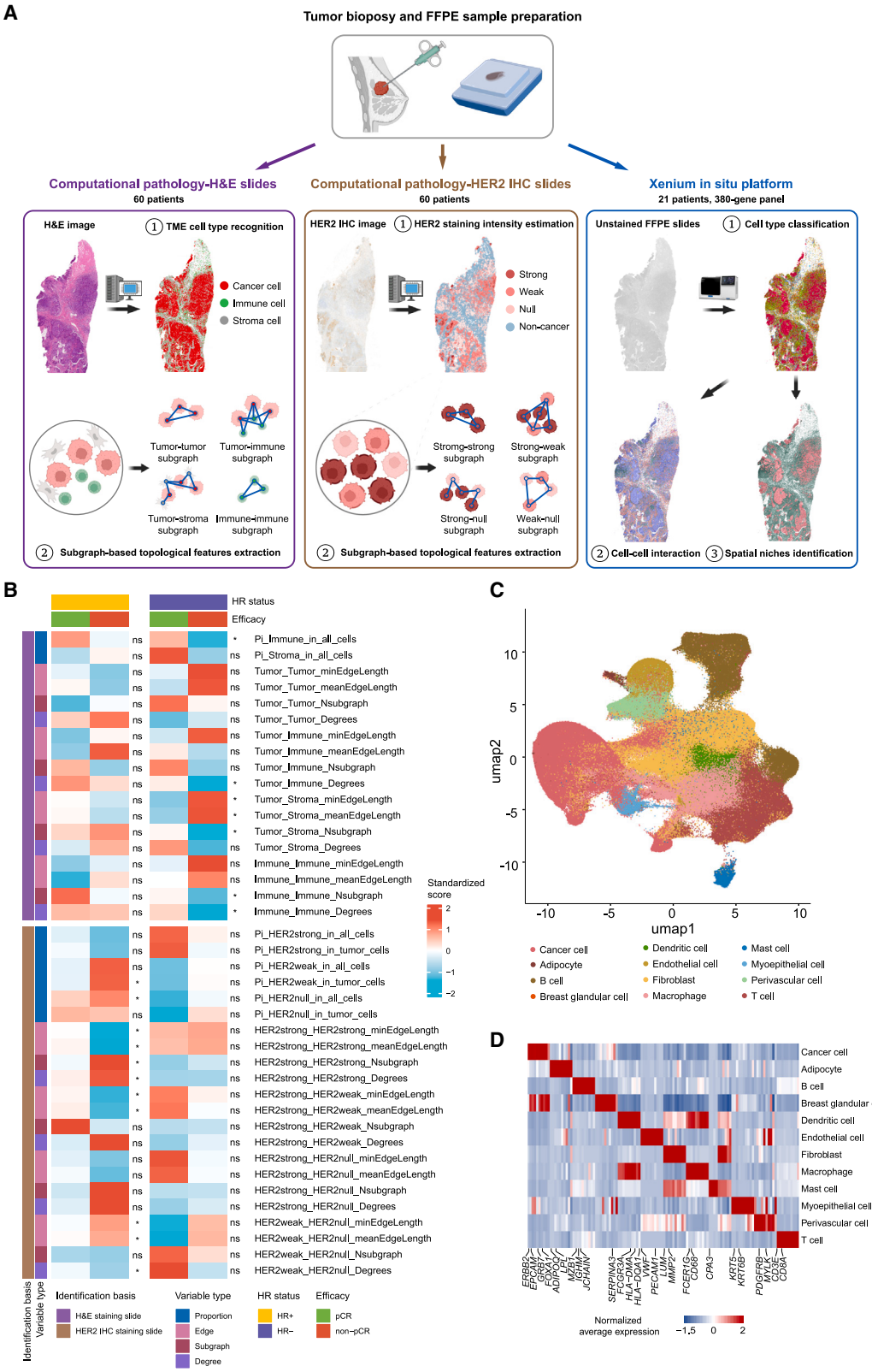

Figure 2. Workflow of spatial analysis: computational pathology and Xenium *in situ* platform

(A) Data generation of spatial profiling. Biopsied tissue was formalin fixed and paraffin embedded (FFPE). With H&E-stained slides, computational pathology identified three main cell types, cancer cells, immune cells and stroma cells. With HER2 IHC slides, computational pathology classified cancer cells into three

(legend continued on next page)

Please cite this article in press as: Ma et al., Spatial determinants of antibody-drug conjugate SHR-A1811 efficacy in neoadjuvant treatment for HER2-positive breast cancer, Cancer Cell (2025), https://doi.org/10.1016/j.ccell.2025.03.017

interest from 12 HR+ patients (7 pCR and 5 non-pCR) and 9 HR− patients (4 pCR and 5 non-pCR) (Figure 2A), resulting in high-quality data comprising over 2 million cells (Table S5). Our 380-gene panel included 280 manufacturer-recommended breast cancer genes and 100 custom genes (Table S6). From the Xenium data, we identified robust specific cell types, which were also validated using H&E-stained images from the same Xenium slides (Figures 2C and 2D).

Cancer cell-cytotoxic T cell interactions as a key factor for the SHR-A1811 response in the HR– subgroup

As indicated by computational pathology analysis, the proportion of immune cells (Pi_Immune_in_all_cells) was the variable that was most significantly correlated with treatment efficacy in the HR− subgroup ($p = 0.02$, Figures 2B, 3A, and 3B). Nevertheless, a significant difference was not observed in the HR+ subgroup ($p = 0.32$, Figure 3A). Furthermore, to identify specific immune cell types that were the main contributors to treatment response, we used Xenium data. Among all major cell types, a significantly higher proportion of T cells was observed in patients who achieved a pCR ($p = 0.011$, Figure 3C). After subdividing T cells into subgroups, all T cell subgroups were more abundant in the pCR group, of which cytotoxic T cells showed the greatest difference in proportion between pCR tumors and non-pCR tumors (median proportion: 1.6% in non-pCR tumors vs. 4.8% in pCR tumors; Figure 3D). Additionally, at the IHC level, we also confirmed that the intensity of $CD8^+$ T cells, the marker of cytotoxic T cells, was significantly higher in the pCR group within the HR− group ($p = 0.00031$, Figure 3E), while no significant difference was observed in the HR+ group ($p = 0.13$). Furthermore, the enrichment of cytotoxic T cells could also be validated morphologically by higher levels of TILs in HR− pCR tumors ($p = 0.034$) (Figure 1C), which were highly correlated with $CD8^+$ cytotoxic T cells. In contrast, this relationship between $CD8^+$ T cells and treatment efficacy was not observed in our HER2+ FASCINATE-N PCbHP arm in either HR subgroup (Figure S4A). These findings underline the role of the proportion of cytotoxic T cells in the SHR-A1811 response, especially for HR− tumors.

It has been acknowledged that the spatial structure of the tumor immune microenvironment (TIME) affects the treatment response.[17] According to our computational pathology analysis based on H&E-stained WSIs, we detected a tighter tumor-immune connection in patients who achieved a pCR, as indicated by a greater immune-infiltrating landscape in H&E-stained images ($p = 0.023$, Figures 3F, 3G, and 2B). This phenomenon was not significant in HR+ tumors. Thus, we used spatial ligand-receptor (L-R) interaction analysis to identify cell pairs that exhibited strong functional communication. Among all significant L-R pairs across HR− patients, cancer cell (ligand)-cytotoxic T cell (receptor) pairs were the most common (92 pairs), followed by cancer cell (receptor)-cytotoxic T cell (ligand) interactions (76 pairs) (Figure 3H). Specifically, regarding cancer cell (ligand)-cytotoxic T cell (receptor) interactions, the non-pCR group exhibited increased PDCD1LG2 (PDL2)-PDCD1 interactions ($p = 0.043$) and the pCR group exhibited increased HLA-A-CD8A interactions ($p = 0.062$) (Figure 3I). Using multiple immunohistochemistry (mIHC), we further revealed the role of PDCD1-PDCD1LG2 during treatment. We found that the proportion of $PDCD1^+$ cytotoxic T cells in all cytotoxic T cells increased more significantly in the HR− tumors compared with HR+ tumors (Figure S4B). Meanwhile, the proportion of $PDCD1LG2^+$ tumors cells in all tumors showed no significant change in HR− tumors but decreased significantly in HR+ tumors (Figure S4C), suggesting the different remodeling effect of SHR-A1811 toward TIME in different HR subgroups. In addition to L-R analysis, which focuses on the spatial relationships between 2 specific cell types, we also clustered spatial niches that consist of multiple cell subtypes. A total of 6 niches were identified (niches 0 to 5), and all the niches were found in each patient (Figures S4D and S4E). Among all niches, niche 4 was the only one whose proportion was correlated with efficacy, with a higher proportion being prone to pCR ($p = 0.032$, Figure 3J). Compared with the other niches, niche 4 contained the fewest cancer cells and the most cytotoxic T cells (8.2% and 5.2%, respectively) (Table S7). Spatially, niche 4 represented cells infiltrating into cancer cell nests (Figure 3K). And the connection degree between cancer cells and cytotoxic T cells within niche 4 was the highest among all niches (Figure 3L), suggesting a strong interaction between these two cell types, which further highlighted the role of cancer cell-cytotoxic T cell relationships.

In summary, we found that the proportion and spatial interaction of immune cells (particularly cytotoxic T cells) were correlated with the response of breast cancer patients to SHR-A1811, especially HR− patients.

Spatial distribution of HER2+ cancer cells is associated with SHR-A1811 response in HR+ patients

As mentioned previously, cancer cells appear to play a more pivotal role in the efficacy of SHR-A1811 in HR+ patients. And previous studies have highlighted the spatial pattern of HER2 expression to be related with ADC response.[12] Thus, we distinguished the HER2 expression patterns of cancer cells and investigated their spatial distribution as well as topological interactions at the single-cell level, using computational pathology (Figure 2B).

Our findings revealed that for HER2-strong-positive tumors, the spatial connection edge length ($p = 0.0091$, Figure 4A) and the number of subgraphs ($p = 0.016$, Figure 4B) of these cells were significantly associated with poor treatment efficacy, whereas their spatial connection degree was correlated with

groups with strong-positive (HER2-strong), weak-positive (HER2-weak), and null (HER2-null) HER2 intensity, respectively. Xenium profiled transcriptome of unstained FFPE slides using a 380-gene panel in single-cell resolution. Created with BioRender.com.

(B) Heatmap showing all spatial features generated by computational pathology based on standardized scores, including proportion, edge, subgraph, and degree metrics. The comparison of actual scores between the pCR group and the non-pCR group is provided separately for each HR status. Statistical significance was determined using the Wilcoxon test. *$p < 0.05$; ns, not significant.

(C) UMAP projection of major cell types annotated in Xenium profiling.

(D) Heatmap showing the expression of upregulated genes in each Xenium major cell type. Representative gene markers were annotated. See also Figures S2, S3 and Tables S4–S6.

Please cite this article in press as: Ma et al., Spatial determinants of antibody-drug conjugate SHR-A1811 efficacy in neoadjuvant treatment for HER2-positive breast cancer, Cancer Cell (2025), https://doi.org/10.1016/j.ccell.2025.03.017

CellPress

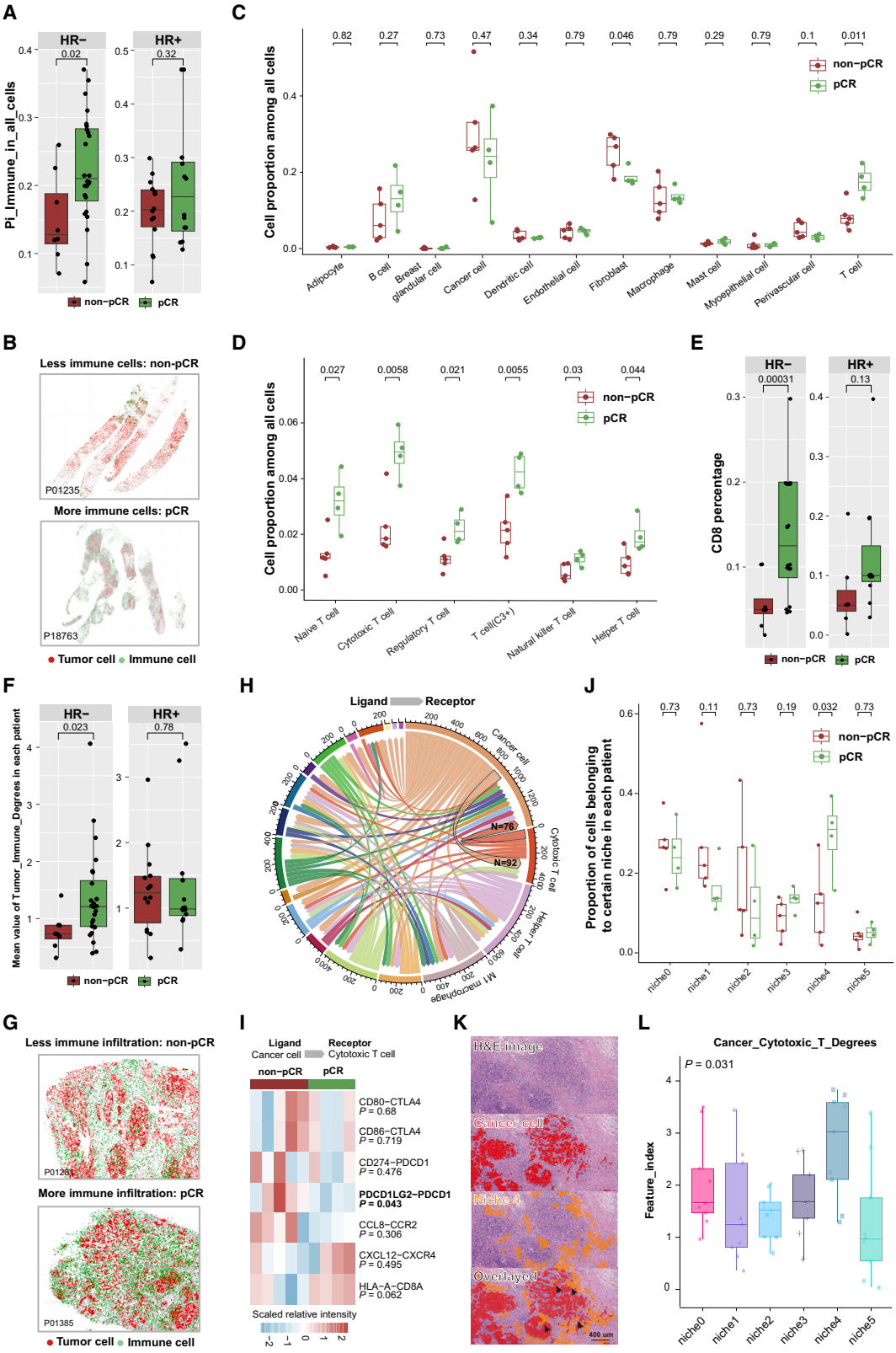

Figure 3. Role of tumor immune microenvironment in the treatment response of HR–/HER2+ breast cancers

(A) Proportion of immune cells among all cells identified by H&E-stained computational pathology between the pCR (n = 25 for HR−, n = 13 for HR+) and non-pCR (n = 8 for HR−, n = 14 for HR+) group. Statistical significance was determined using the Wilcoxon test.

(legend continued on next page)

Please cite this article in press as: Ma et al., Spatial determinants of antibody-drug conjugate SHR-A1811 efficacy in neoadjuvant treatment for HER2-positive breast cancer, Cancer Cell (2025), https://doi.org/10.1016/j.ccell.2025.03.017

improved treatment efficacy (p = 0.05, Figure 4C). Collectively, these indices indicated that tumors with uniformly distributed HER2-strong-positive tumors cell were prone to reach pCR, while those with aggregated distribution were more likely to be non-pCR (Figure 4D).

We further investigated the underlying molecular mechanisms related to the spatial patterns of HER2-strong-positive tumor cells described previously. Using Xenium data, we found that the closeness and aggregation of tumor cells are associated with elevated expression of genes downstream of *ESR1*, such as *PGR* and *CCND1*, encoding cyclin D that binds to CDK4 and CDK6 (Figures 4E and 4F). The enrichment of *PGR* rather than *ESR1* in the non-pCR group could also been verified in the routine IHC tests (Figure 4G). Recently, we reported a HER2-LUM subtype, which represents a subgroup of HER2+ breast cancer that resembles the molecular portraits of HR+/HER2- breast cancer and might benefit from CDK4/6 inhibitors.[18] We found that the HER2-LUM subtype was enriched in the non-pCR group (p = 0.037, Figure 4H). We then analyzed the correlation between the spatial patterns of HER2-strong-positive tumor cells and the HER2-LUM subtype. The results showed that the closeness and aggregation of HER2-strong-positive tumor cells were significantly related to the HER2-LUM subtype (Figure 4I), which could also be observed in an independent dataset (Figure S5A). Additionally, in the independent dataset, we also found that the closeness and aggregation of HER2-strong-positive tumor cells was more correlated with *PGR* expression than *ESR1* expression (Figure S5B). These results indicated that a luminal-like molecular background might contribute to aggregated distribution of HER2-strong-positive tumor cells. Moreover, we found that in the non-pCR group, while the proportion of HER2-strong-positive tumor cells significantly decreased in both HR subgroups, the reduction was less pronounced in the HR+ subgroup (Figure S5C). In addition, patients with highest proportion of HER2-strong-positive tumor cells at surgery were all classified as HER2-LUM subtype at baseline (Figure S5C), suggesting that the luminal-like molecular feature of HER2-strong-positive tumor cells might affect response to SHR-A1811.

We additionally analyzed the heterogeneity in HER2 expression to explore its predictive value for SHR-A1811 efficacy. We found that a higher proportion of HER2-weak (Figure S5D) and HER2-weak plus HER2-null (Figure S5E) tumor cells was significantly correlated with non-pCR results, particularly in HR+ patients. And tumors with highest HER2-weak plus HER2-null proportion were all classified as HER2 IHC score 2+, consistent with our findings displayed in Figure 2B. Moreover, the relation between the proportion of HER2-weak cells and SHR-A1811 efficacy seemed to be stronger than the proportion of HER2-weak plus HER2-null cells, which suggested the value of identifying HER2 intensity precisely.

Construction of an SHR-A1811 efficacy prediction model using multimodal data and ensemble learning algorithms

Prediction of the response to ADCs and their precise administration remains a vital concern in clinical practice. We developed an innovative efficacy prediction model for SHR-A1811, integrating our findings on spatial heterogeneity, which represented an exploratory analysis to construct an easy-to-use AI-based model for a novel ADC. As depicted in Figure 5A, we leveraged readily accessible clinical data and pathological WSIs (paired H&E-stained and HER2 IHC-stained slides of pretreatment core needle biopsies) for data acquisition. First, advanced computational pathology techniques were employed to extract cellular proportions and topological features from these WSIs as described previously. Subsequently, we integrated these data with clinical and pathological information to construct a multidimensional efficacy prediction model. With this, we constructed an efficacy prediction model (Figure 5B). We employed

(B) Representative H&E-stained computational pathology images with low (upper panel, patient P01235) and high (lower panel, patient P18763) proportion of immune cells, respectively. Cell types were identified using Hover-Net.
(C) Proportion of major cell types in all cells derived from Xenium data between the pCR (n = 4) and non-pCR (n = 5) group in the HR− subgroup. Statistical significance was determined using the Wilcoxon test.
(D) Proportion of specific T cell subtypes in all cells derived from Xenium data between the pCR (n = 4) and non-pCR (n = 5) group in the HR− subgroup. Statistical significance was determined using the Wilcoxon test.
(E) Comparison of CD8 IHC intensity between the pCR (n = 20 for HR−, n = 11 for HR+) and non-pCR (n = 8 for HR−, n = 7 for HR+) group. Statistical significance was determined using the Wilcoxon test.
(F) Spatial connection degree of tumor cells and immune cells (higher value meaning more connected) identified by H&E-stained computational pathology between the pCR (n = 25 for HR−, n = 13 for HR+) and non-pCR (n = 8 for HR−, n = 14 for HR+) group. Statistical significance was determined using the Wilcoxon test.
(G) Representative H&E-stained computational pathology images with high (upper panel, patient P01281) and low (lower panel, patient P01385) connection degree of tumor cells and immune cells, respectively. Cell types were identified using Hover-Net.
(H) Chord diagram showing the number of significant ligand-receptor interaction pairs between two specific cell subtypes across all HR− patients. Interactions with adjusted p value less than 0.05 were considered significant. p values were derived from spatial cell-level ligand-receptor interaction analysis (STAR Methods). The width of the arrow represents the number of pairs. The direction of arrow represents the ligand cell (start of the arrow) and receptor cell (end of the arrow). Those ligand-receptor interaction pairs whose total number cross all HR− patients less than 30 were not indicated.
(I) Heatmap showing the canonical ligand-receptor interaction between cancer cell (ligand) and cytotoxic T cell (receptor) in the spatial ligand-receptor analysis. Statistical significance was determined using the Wilcoxon test.
(J) Comparison of proportion of cells included in different spatial niches between the pCR group (n = 4) and the non-pCR group (n = 5). Statistical significance was determined using the Wilcoxon test.
(K) Representative images showing the distribution of cancer cells and niche 4 cells. Arrows indicated cells in niche 4 that infiltrated in tumor cell nests.
(L) Comparison of the spatial connection degree of cancer cells and cytotoxic T cells identified by Xenium (n = 9) across different niches.
Statistical significance was determined using the Kruskal-Wallis test across all niches. In boxplots (A, C–F, J, and L), the centerline represents the median, the box limits represent the upper and lower quartiles, the whiskers represent the 1.5× interquartile range, and the points represent individual samples. See also Figure S4 and Table S7.

Please cite this article in press as: Ma et al., Spatial determinants of antibody-drug conjugate SHR-A1811 efficacy in neoadjuvant treatment for HER2-positive breast cancer, Cancer Cell (2025), https://doi.org/10.1016/j.ccell.2025.03.017

CellPress

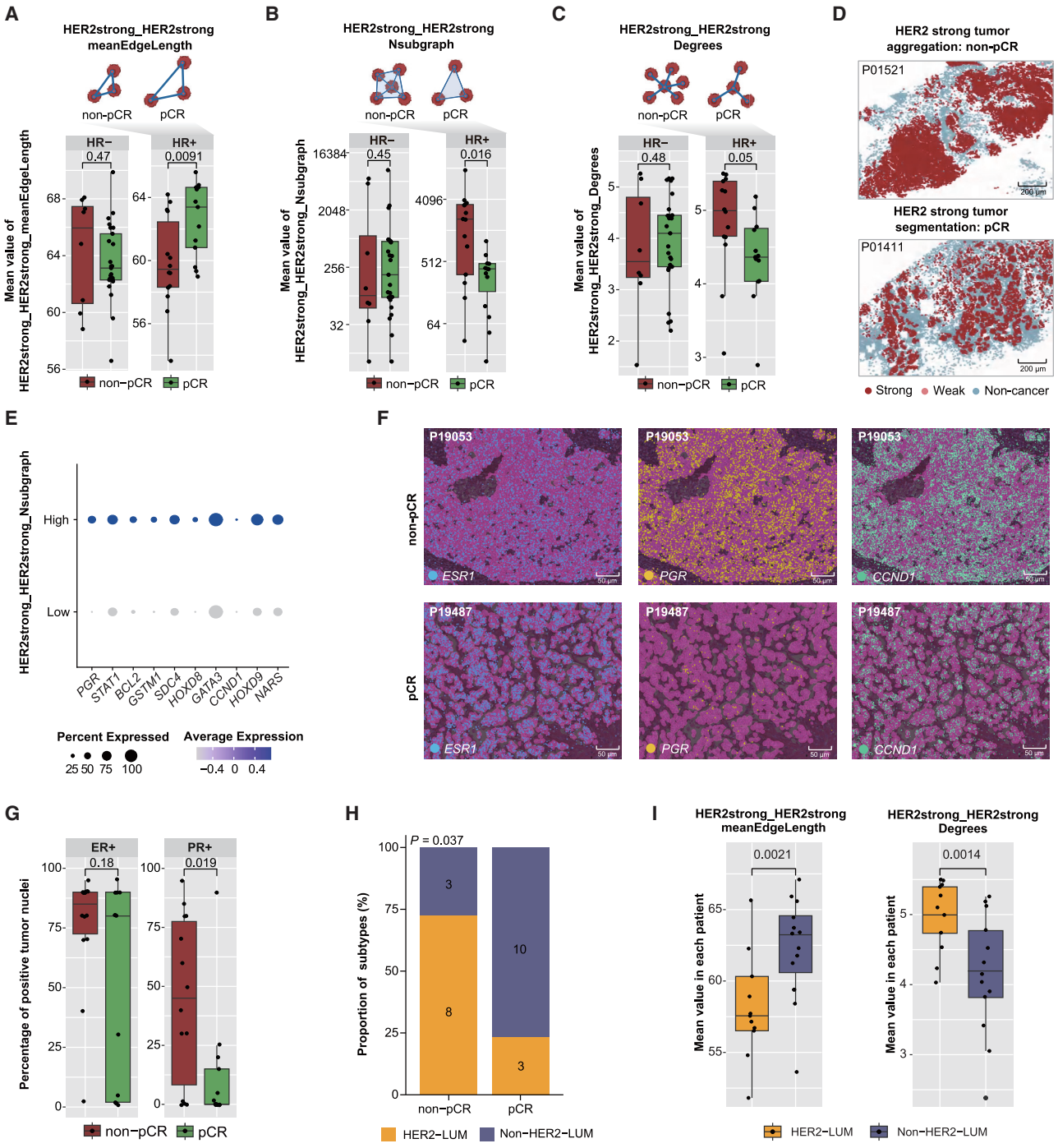

Figure 4. Relation between characteristics of HER2-positive cancer cells and treatment response in HR+/HER2+ breast cancers

(A) Comparison of mean connection edge length by HER2-strong-positive and HER2-strong-positive tumor cells identified by HER2 IHC computational pathology between the pCR (n = 25 for HR−, n = 13 for HR+) and non-pCR (n = 8 for HR−, n = 14 for HR+) group. Statistical significance was determined using the Wilcoxon test.

(B) Comparison of number of subgraphs (higher value meaning larger aggregation scales) between HER2-strong-positive and HER2-strong-positive tumor cells identified by HER2 IHC computational pathology between the pCR (n = 25 for HR−, n = 13 for HR+) and non-pCR (n = 8 for HR−, n = 14 for HR+) group. Statistical significance was determined using the Wilcoxon test.

(C) Comparison of spatial connection degree (higher value meaning more connected) by HER2-strong-positive and HER2-strong-positive tumor cells identified by HER2 IHC computational pathology between the pCR (n = 25 for HR−, n = 13 for HR+) and non-pCR (n = 8 for HR−, n = 14 for HR+) group. Statistical significance was determined using the Wilcoxon test.

(legend continued on next page)

Please cite this article in press as: Ma et al., Spatial determinants of antibody-drug conjugate SHR-A1811 efficacy in neoadjuvant treatment for HER2-positive breast cancer, Cancer Cell (2025), https://doi.org/10.1016/j.ccell.2025.03.017

stratified sampling based on clinicopathological characteristics to create a training set and a testing set from 60 patients who received SHR-A1811, utilizing a 7:3 ratio for the division (Table S8). A real-world neoadjuvant novel anti-HER2 ADC cohort comprising 54 patients was also included as an independent validation cohort (Table S9). Furthermore, patients from the PCbHP cohort in our HER2+ FASCINATE-N trial were included to validate the specificity of the model for non-ADC treatment (Table S9). Detailed information of these cohorts is provided in the STAR Methods section and Tables S8 and S9.

For variable selection, to prevent overfitting and improve the model's robustness and generalizability, we performed a feature selection process in model construction (Figure S6A). We began with 40 variables, consisting of 2 clinicopathological variables and 38 digital pathology variables. We first excluded 11 collinear variables which can obscure the independent contributions of each variable to predict outcome. Then, we performed weak correlation removal to exclude 16 variables with minimal association to the outcome to diminish noise from irrelevant features and to further reduce the risk of overfitting. Ultimately, 13 variables that showed the strongest and most independent associations with efficacy were retained in the final model. Most of these variables demonstrated significant associations with efficacy, as previously discussed, and Shapley additive explanations (SHAP) analysis confirmed their predictive value (Figure 5C). Detailed information regarding model integration and optimization is provided in the STAR Methods section.

Our model demonstrated robust performance of the efficacy prediction in the SHR-A1811 training and testing datasets (training set AUC = 0.95, 95% confidence interval [CI]: 0.89–1.00; testing set AUC = 0.86, 95% CI: 0.76–1.00) (Figures 5D and 5E). It also exhibited strong performance in the real-world ADC validation dataset (AUC = 0.83, 95% CI: 0.68–1.00) (Figure 5F). The PCbHP group had the lowest performance (AUC = 0.62, 95% CI: 0.42–0.82) (Figure 5G), showing that the model was specific to ADC treatment response prediction rather than conventional dual-targeted PCbHP therapy. Finally, confusion matrices further demonstrated the model's effective predictive performance on the both SHR-A1811 datasets and the real-world ADC dataset (Figure S6B).

Overall, our comprehensive workflow for predicting SHR-A1811 efficacy proved its potential for clinical application in HER2+ breast cancer patients.

DISCUSSION

In this study, we conducted a translational study based on prospectively collected omics data from the SHR-A1811 arm of the phase 2 FASCINATE-N trial to identify biomarkers for this novel anti-HER2 ADC with specific spatial parameters. We found that treatment efficacy in the HR− group was linked to the TME, particularly the presence and distribution of immune cells (i.e., TILs, particularly cytotoxic T cells). Conversely, treatment response in the HR+ group showed stronger dependence on tumor cellular features, particularly spatial distribution patterns. Specifically, clustered gathering of HER2-strong-positive cells (as opposed to uniformly distributed) were associated with poorer therapeutic outcome. This distinct spatial pattern was associated with tumor molecular properties similar to those of luminal-like breast cancer. We also tried to create a model that predicts treatment outcomes for SHR-A1811, which also showed potential in predicting the treatment response of other novel ADCs.

Given the rapid advancements in anti-HER2 treatments, there is a growing need for biomarker and prediction tools to guide precise patient management, balancing efficacy, toxicity, and cost. HER2DX, an mRNA-based tool, has been developed and validated for trastuzumab-based treatment.[19,20] It has also demonstrated predictive capabilities in the T-DM1 cohort.[21] However, biomarkers for novel ADCs remain in the early stages of investigation. These novel ADCs differ significantly from T-DM1 in their design, including distinct payloads, higher DARs, and degradable linkers, necessitating unique biomarker considerations.[22] In our study, we focused on the neoadjuvant SHR-A1811 monotherapy cohort to explore potential biomarkers. Previous research in advanced breast cancer has suggested that specific spatial expression patterns of HER2 may correlate with the treatment response to novel ADCs such as T-DXd.[12] We hypothesize that computational pathology, which considers not only HER2-expressing cancer cells but also the TME and their interactions, can enhance our understanding of the SHR-A1811 treatment response. Leveraging digital pathology offers high accessibility and cost-effectiveness, making it suitable for future clinical implementation. Additionally, Xenium technology provides detailed interpretations and evidence related to spatial structural features relevant to treatment efficacy. Therefore, combining digital pathology with an *in-situ* gene expression assay could provide valuable insights into the spatial biomarkers associated with SHR-A1811.

(D) Representative HER2 IHC-stained computational pathology images of HER2-strong-positive tumor cells with low (upper panel) and high (lower panel) level of closeness and aggregation. Cell types were identified using D-PathAI.
(E) Dot plot showing top 10 upregulated genes in cancer cells from patients with higher number of subgraphs between HER2-strong-positive and HER2-strong-positive tumor cells compared with those with lower number of subgraphs.
(F) Comparison of *in-situ ESR1*, *PGR*, and *CCDN1* expression on cancer cells (highlighted in magenta) between the pCR and non-pCR group.
(G) Comparison of the percentage of ER and PR positive tumor cells identified by IHC staining between the pCR ($n = 13$) and non-pCR ($n = 14$) group. ER, estrogen receptor; PR, progesterone receptor. Statistical significance was determined using the Wilcoxon test.
(H) Percentage bar chart comparing the proportion of the HER2-LUM subtypes in pCR and non-pCR in the HR+ subgroup. Number in the bars represent sample/patient numbers. Statistical significance was calculated by comparing the proportions of HER2-LUM subtypes and non-HER2-LUM subtypes between the pCR and non-pCR groups within the HR+ subgroup using Fisher's exact test.
(I) Comparison of mean connection edge length and spatial connection between of HER2-strong-positive and HER2-strong-positive tumor cells of HER2-LUM subtype ($n = 11$) and non-HER2-LUM subtype ($n = 13$) in the HR+ subgroup. Statistical significance was determined using the Wilcoxon test. In boxplots (A–C, G, and I), the centerline represents the median, the box limits represent the upper and lower quartiles, the whiskers represent the 1.5× interquartile range, and the points represent individual samples. See also Figure S5.

Please cite this article in press as: Ma et al., Spatial determinants of antibody-drug conjugate SHR-A1811 efficacy in neoadjuvant treatment for HER2-positive breast cancer, Cancer Cell (2025), https://doi.org/10.1016/j.ccell.2025.03.017

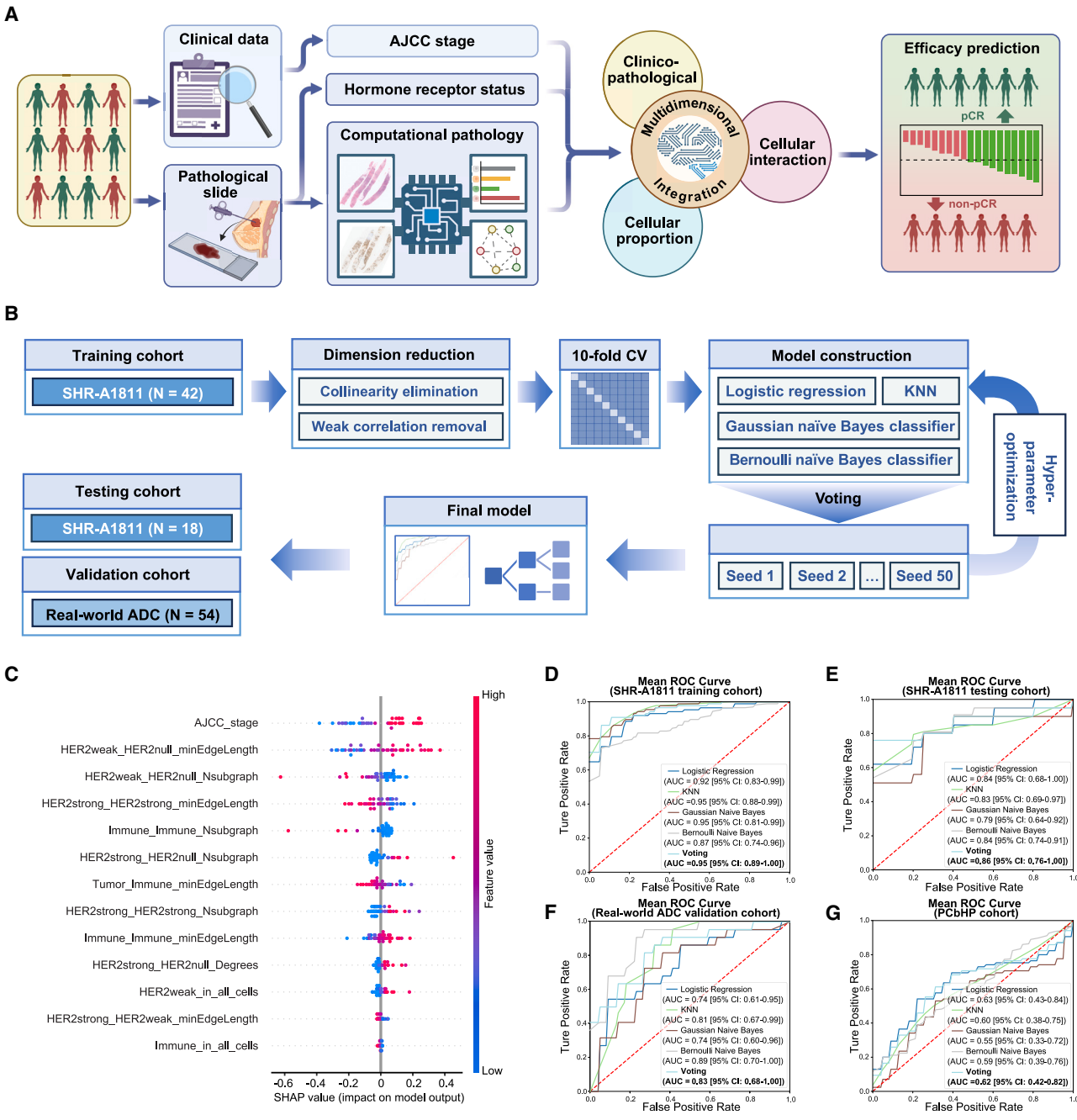

Figure 5. Establishment of SHR-A1811 efficacy prediction model using multi-modal data and ensemble learning algorithms

(A) Schematic diagram of multi-dimensional data integration for constructing the efficacy prediction model. AJCC, American Joint Committee on Cancer. Created with BioRender.com.

(B) A flowchart detailing the framework for efficacy prediction model development involving stratification of training and validation datasets, variable selection, multimodal ensemble, and modal optimization. CV, cross-validation; KNN, k-nearest neighbor algorithm.

(C) Visualization of predictive value for each variable considered in the final model construction, represented by SHAP (Shapley additive explanations) values of each sample in the SHR-A1811 training set.

(D–G) Comparison of the area under curve (AUC) of the receiver operating characteristic (ROC) curves for various models (including logistic regression model, k-nearest neighbor model, Gaussian naive Bayes model, and Bernoulli naive Bayes model) and ensemble voting model in SHR-A1811 training set (n = 42) (D), SHR-A1811 validation set (n = 18) (E), real-world ADC set (n = 54) (F), and PCbHP set (n = 60) (G). See also Figure S6 and Tables S8 and S9.

Please cite this article in press as: Ma et al., Spatial determinants of antibody-drug conjugate SHR-A1811 efficacy in neoadjuvant treatment for HER2-positive breast cancer, Cancer Cell (2025), https://doi.org/10.1016/j.ccell.2025.03.017

This study revealed that immune cells in the TIME, particularly cytotoxic T cells, play a significant role in the response of breast cancer patients to SHR-A1811, which seemed to depend on HR status. Notably, this association demonstrated stronger relevance in HR−/HER2+ patients. It has long been reported that TIME is an important component of treatment response in breast cancer of different HR status. For instance, high TIL levels correlated with improved survival outcomes in triple-negative breast cancers but was related with unfavorable outcomes in luminal breast cancers.[23] Within HER2+ breast cancer, TILs were also discovered to be an independent prognostic factor in HR− rather than in HR+ breast cancers.[24] This study further provided evidence for the role of TILs in the context of novel ADC treatments for HER2+ breast cancers. The divergent roles of TILs across HR subtypes as biomarkers for prognosis and treatment response highlight a critical interplay between HR status, TIME, and treatment response. However, it is worth mentioning that we also found a tendency of higher TILs in the HR+ non-pCR group, where a statistical significance was not reached, possibly due to small sample size. Increasing evidence suggests that some of HR+ tumors are similar to triple-negative breast cancers, such as some luminal B diseases,[25] which obscures the role of TILs between different HR status. Hence, further large-scale studies are needed to investigate the role of TILs in anti-HER2 ADC treatment in the HR+ subgroup.

Both the cancer-immune relationship in H&E-stained images and the niche 4 in Xenium analysis suggest the rationale that, the effect of immune cells on the SHR-A1811 response is determined not only by their quantity but also by their spatial interactions with cancer cells. Taken together, these findings expanded the understanding of the role of tumor immunology-spatial structure interactions in anti-HER2 ADC treatment.

Currently, the role of the TIME in the response of breast cancer to novel anti-HER2 ADCs is obscure. Clinical trial-based evidence primarily came from the DAISY trial,[12] which tested the safety and efficacy of T-DXd in advanced HER2+ breast cancers. Based on a machine learning model developed with HER2 IHC-stained images, DAISY identified a spatial pattern named cluster 6 enriched in non-response patients, characterized by lower HER2 staining, moderate cell density, and abundant fibroblasts and immune cells. In this study, we included both HER2 IHC-stained images and H&E-stained images, and firstly identified single cells subsequent analysis, which orchestrated the single-cell *in situ* imaging technology. This strategy provided a methodology to characterize spatial structure precisely and quantitatively, and supported the construction of a more interpretable efficacy prediction model. As for pre-clinical studies, in an immunocompetent mouse model bearing human HER2-expressing colon cancer cells, Tomomi et al. reported that T-DXd treatment can fortify anti-tumor immunity by increasing antigen presentation via major histocompatibility complex (MHC) class I, and upregulating the proportion of tumor-infiltrating dendritic cells and $CD8^+$ T cells. The combination of T-DXd and an anti-PD-1 antibody was more potent than either monotherapy.[26] These results echoed our finding that in neoadjuvant SHR-A1811 monotherapy, pretreatment of tumors with more abundant cytotoxic T cells (i.e., $CD8^+$ T cells) and stronger HLA class I-CD8 interactions were more likely to achieve pCR. In contrast, non-pCR tumors showed fewer cytotoxic T cells and more PDL2-PD1 interactions. In addition, we found the significant increase of $PDCD1^+$ cytotoxic T cells after treatments in the non-pCR group, which also suggested the potential value of combining anti-PD-1 immunotherapy.

We also found that the proximity and aggregation of HER2-strong-positive tumor cells indicated a lower pCR rate in the HR+ subgroup. This distribution pattern may be partially attributed to the presence of tumor cells exhibiting glandular structures, which was more often observed in HR+/HER2− breast cancer with low histological grade.[27] Additionally, we found that HER2-LUM subtypes were enriched in the non-pCR group, which were a subgroup of HER2+ breast mimicking HR+/HER2− disease molecularly.[18] On the one hand, the upregulation of the ER pathway has been linked to poor responses to trastuzumab and chemotherapy, potentially explaining the reduced treatment response in this tumor group. On the other hand, another hypothesis is that the closeness and aggregation of cancer cells may directly impact the treatment response to novel ADCs because the spatial distribution of tumor cells may influence drug diffusion and bystander effect. Notably, while the underlying cause-and-effect relationship requires further investigation, our previous findings that HER2-LUM tumors responded well to CDK4/6 inhibitors suggest that combining other therapies, such as CDK4/6 inhibitors, may be beneficial to this group of diseases.[18]

To address the limitations of previous studies that lacked adequate tools for the precise administration of novel ADCs, we developed a predictive model with solid clinical applicability. This model leverages high-resolution digital scans of routine pre-treatment H&E-stained and HER2 IHC-stained sections, combined with clinical staging and HR status, to extract key features for modeling. Our approach comprehensively reveals and summarizes critical factors within the TME and the spatial distribution characteristics of target cells that impact ADC efficacy. The predictive model achieved an AUC exceeding 0.8, underscoring the value of spatial factors within the TME and the intratumoral HER2 heterogeneity in the prediction of treatment efficacy. SHAP model interpretability analysis further confirmed the significant contribution of these factors to the model's performance. Additionally, we extended our model to other novel ADCs. This might be attributed to the pharmacological similarities of these ADCs. In summary, the predictive model developed in this study shows promise as an effective tool for predicting the efficacy of SHR-A1811, with significant potential for clinical application.

Limitations of the study

This study has some limitations. Despite our efforts in mitigating overfitting risks and constructing a more reliable model by combining feature selection, ensemble modeling, and robust validation strategies,[28–30] our model was based on a relatively small sample size. Additional studies with more patients are needed to strengthen these findings. And while our study provides a descriptive analysis, it does not delve deeply into the underlying mechanisms involved. For instance, future investigations should elucidate why a uniform distribution of HER2-strong-positive tumor cells, rather than a clustered arrangement, is correlated with an enhanced treatment response. Elucidating these questions could ultimately improve the management of SHR-A1811 and related ADCs.

RESOURCE AVAILABILITY

Lead contact

Requests for further information and resources should be directed to and will be fulfilled by the lead contact, Zhi-Ming Shao (zhimingshao@fudan.edu.cn).

Materials availability

This study did not generate new unique reagents.

Data and code availability

WGS, targeted sequencing, RNA-sequencing, and Xenium data generated by this study have been deposited at NGDC (National Genomics Data Center, https://ngdc.cncb.ac.cn/) with the BioProject number PRJCA036177 (WGS and targeted sequencing: OMIX009380, RNA-sequencing: OMIX009381, and Xenium data: OMIX009059) and are publicly available. Xenium data are also deposited at NODE (The National Omics Data Encyclopedia, https://www.biosino.org/node/index) with the accession number OEP00006015 and are publicly available. H&E-stained WSIs of the TCGA-BRCA cohort were downloaded from Cancer Imaging Archive (https://www.cancerimagingarchive.net/collection/her2-tumor-rois/). RNA-seq of the TCGA-BRCA cohort were downloaded from cBioPortal (https://www.cbioportal.org/). All codes used for the data analysis, along with the details of the published software packages for data processing, are listed in the key resources table. No new code or mathematical algorithms were generated from this manuscript. Any additional information required to reanalyze the data reported in this paper is available from the lead contact upon request.

ACKNOWLEDGMENTS

This work was supported by grants from the National Key Research and Development Project of China (2024YFA1107400), the National Natural Science Foundation of China (92159301, 82425044, 82441028, 82473216, 82272704, 82341003, and 82072921), the Outstanding Youth Medical Talents of Shanghai (WJWRC202306), the Shanghai Municipal Health Commission Excellence Project for Health Industry Research (20244Z0016), the Foundation of the Shanghai Municipal Education Commission (24RGZNA03), the Shanghai Key Laboratory of Breast Cancer (12DZ2260100), and the Shanghai Rising-Star Program (23QA1401400). Yi-Zhou Jiang is a SANS Exploration Scholar. The funders had no role in the study design, data collection and analysis, decision to publish, or preparation of the manuscript. This study is also supported by the Human Phenome Data Center of Fudan university.

AUTHOR CONTRIBUTIONS

Conceptualization, Z.-M.S., Y.-Z.J., D.M., and Y.X.; methodology, D.M., L.-J.D., X.-R.W., C.-L.L., S.Z., H.Z., L.C., Y.-Z.Z., and L.Y.; software, S.Z., Y.-Z.Z., and L.Y.; formal analysis, D.M., L.-J.D., X.-R.W., C.-L.L., and H.Z.; resources, Z.-M.S., Y.-Z.J., J.-J.L., L.C., W.-T.Y., and T.Z.; data curation, D.M., L.-J.D., X.-R.W., C.-L.L., H.Z., and M.L.; writing – original draft, D.M., L.-J.D., X.-R.W., and C.-L.L.; writing – review & editing, D.M., L.-J.D., X.-R.W., and C.-L.L.; visualization, D.M., L.-J.D., X.-R.W., and C.-L.L.; supervision, Z.-M.S. and Y.-Z.J.; project administration, Y.-Z.J., D.M., and Y.X.; funding acquisition, Z.-M.S., Y.-Z.J., and D.M.

DECLARATION OF INTERESTS

The authors declare no competing interests.

STAR★METHODS

Detailed methods are provided in the online version of this paper and include the following:

SUPPLEMENTAL INFORMATION

Supplemental information can be found online at https://doi.org/10.1016/j.ccell.2025.03.017.

Received: August 9, 2024
Revised: December 17, 2024
Accepted: March 12, 2025
Published: April 10, 2025

REFERENCES

1. Wang, L., Li, M., and Hwang, T.H. (2024). The 3D Revolution in Cancer Discovery. Cancer Discov. *14*, 625–629. https://doi.org/10.1158/2159-8290.CD-23-1499.
2. Loibl, S., and Gianni, L. (2017). HER2-positive breast cancer. Lancet *389*, 2415–2429. https://doi.org/10.1016/S0140-6736(16)32417-5.
3. Oh, D.-Y., and Bang, Y.-J. (2020). HER2-targeted therapies - a role beyond breast cancer. Nat. Rev. Clin. Oncol. *17*, 33–48. https://doi.org/10.1038/s41571-019-0268-3.
4. Curigliano, G., Dunton, K., Rosenlund, M., Janek, M., Cathcart, J., Liu, Y., Fasching, P.A., and Iwata, H. (2023). Patient-reported outcomes and hospitalization data in patients with HER2-positive metastatic breast cancer receiving trastuzumab deruxtecan or trastuzumab emtansine in the phase III DESTINY-Breast03 study. Ann. Oncol. *34*, 569–577. https://doi.org/10.1016/j.annonc.2023.04.516.
5. Hurvitz, S.A., Hegg, R., Chung, W.P., Im, S.A., Jacot, W., Ganju, V., Chiu, J.W.Y., Xu, B., Hamilton, E., Madhusudan, S., et al. (2023). Trastuzumab deruxtecan versus trastuzumab emtansine in patients with HER2-positive metastatic breast cancer: updated results from DESTINY-Breast03, a randomised, open-label, phase 3 trial. Lancet *401*, 105–117. https://doi.org/10.1016/S0140-6736(22)02420-5.
6. Modi, S., Jacot, W., Yamashita, T., Sohn, J., Vidal, M., Tokunaga, E., Tsurutani, J., Ueno, N.T., Prat, A., Chae, Y.S., et al. (2022). Trastuzumab Deruxtecan in Previously Treated HER2-Low Advanced Breast Cancer. N. Engl. J. Med. *387*, 9–20. https://doi.org/10.1056/NEJMoa2203690.
7. Bardia, A., Hu, X., Dent, R., Yonemori, K., Barrios, C.H., O'Shaughnessy, J.A., Wildiers, H., Pierga, J.Y., Zhang, Q., Saura, C., et al. (2024). Trastuzumab Deruxtecan after Endocrine Therapy in Metastatic Breast Cancer. N. Engl. J. Med. *391*, 2110–2122. https://doi.org/10.1056/NEJMoa2407086.
8. Zuo, W.J., Chen, L., Shen, Y., Wang, Z.H., Liu, G.Y., Yu, K.D., Di, G.H., Wu, J., Li, J.J., and Shao, Z.M. (2024). Rational and trial design of FASCINATE-N: a prospective, randomized, precision-based umbrella trial. Ther. Adv. Med. Oncol. *16*, 17588359231225032. https://doi.org/10.1177/17588359231225032.
9. Zhang, T., You, L., Xu, J., Yin, J., Qu, B., Mao, Y., Fu, B., Cao, D., Zhao, L., Feng, J., et al. (2023). Abstract lb031: shr-A1811, a novel anti-her2 adc with superior bystander effect, optimal dar and favorable safety profiles. Cancer Res. *83*, LB031.
10. Yao, H., Yan, M., Tong, Z., Wu, X., Ryu, M.H., Park, J.J., Kim, J.H., Zhong, Y., Zhao, Y., Voskoboynik, M., et al. (2024). Safety, Efficacy, and Pharmacokinetics of SHR-A1811, a Human Epidermal Growth Factor Receptor 2-Directed Antibody-Drug Conjugate, in Human Epidermal Growth Factor Receptor 2-Expressing or Mutated Advanced Solid

Tumors: A Global Phase I Trial. J. Clin. Oncol. *42*, 3453–3465. https://doi.org/10.1200/JCO.23.02044.

11. Zhao, S., Chen, D.P., Fu, T., Yang, J.C., Ma, D., Zhu, X.Z., Wang, X.X., Jiao, Y.P., Jin, X., Xiao, Y., et al. (2023). Single-cell morphological and topological atlas reveals the ecosystem diversity of human breast cancer. Nat. Commun. *14*, 6796. https://doi.org/10.1038/s41467-023-42504-y.
12. Mosele, F., Deluche, E., Lusque, A., Le Bescond, L., Filleron, T., Pradat, Y., Ducoulombier, A., Pistilli, B., Bachelot, T., Viret, F., et al. (2023). Trastuzumab deruxtecan in metastatic breast cancer with variable HER2 expression: the phase 2 DAISY trial. Nat. Med. *29*, 2110–2120. https://doi.org/10.1038/s41591-023-02478-2.
13. Li, H., Xu, Z., Zhou, M., Shi, X., Kang, Y., Bu, Q., Lv, H., Li, M., Lin, M., Cui, L., et al. (2023). In Segment Membranes and Nuclei from Histopathological Images via Nuclei Point-Level Supervision. held in Cham, H. Greenspan, A. Madabhushi, P. Mousavi, S. Salcudean, J. Duncan, T. Syeda-Mahmood, and R. Taylor, eds. (Springer Nature Switzerland)), pp. 539–548.
14. Farahmand, S., Fernandez, A.I., Ahmed, F.S., Rimm, D.L., Chuang, J.H., Reisenbichler, E., and Zarringhalam, K. (2022). Deep learning trained on hematoxylin and eosin tumor region of Interest predicts HER2 status and trastuzumab treatment response in HER2+ breast cancer. Mod. Pathol. *35*, 44–51. https://doi.org/10.1038/s41379-021-00911-w.
15. Jiang, Y.Z., Ma, D., Jin, X., Xiao, Y., Yu, Y., Shi, J., Zhou, Y.F., Fu, T., Lin, C.J., Dai, L.J., et al. (2024). Integrated multiomic profiling of breast cancer in the Chinese population reveals patient stratification and therapeutic vulnerabilities. Nat. Cancer *5*, 673–690. https://doi.org/10.1038/s43018-024-00725-0.
16. Janesick, A., Shelansky, R., Gottscho, A.D., Wagner, F., Williams, S.R., Rouault, M., Beliakoff, G., Morrison, C.A., Oliveira, M.F., Sicherman, J.T., et al. (2023). High resolution mapping of the tumor microenvironment using integrated single-cell, spatial and in situ analysis. Nat. Commun. *14*, 8353. https://doi.org/10.1038/s41467-023-43458-x.
17. Fu, T., Dai, L.J., Wu, S.Y., Xiao, Y., Ma, D., Jiang, Y.Z., and Shao, Z.M. (2021). Spatial architecture of the immune microenvironment orchestrates tumor immunity and therapeutic response. J. Hematol. Oncol. *14*, 98. https://doi.org/10.1186/s13045-021-01103-4.
18. Li, Y.W., Dai, L.J., Wu, X.R., Zhao, S., Xu, Y.Z., Jin, X., Xiao, Y., Wang, Y., Lin, C.J., Zhou, Y.F., et al. (2024). Molecular Characterization and Classification of HER2-Positive Breast Cancer Inform Tailored Therapeutic Strategies. Cancer Res. *84*, 3669–3683. https://doi.org/10.1158/0008-5472.Can-23-4066.
19. Prat, A., Guarneri, V., Paré, L., Griguolo, G., Pascual, T., Dieci, M.V., Chic, N., González-Farré, B., Frassoldati, A., Sanfeliu, E., et al. (2020). A multivariable prognostic score to guide systemic therapy in early-stage HER2-positive breast cancer: a retrospective study with an external evaluation. Lancet Oncol. *21*, 1455–1464. https://doi.org/10.1016/S1470-2045(20)30450-2.
20. Waks, A.G., Ogayo, E.R., Paré, L., Marín-Aguilera, M., Brasó-Maristany, F., Galván, P., Castillo, O., Martínez-Sáez, O., Vivancos, A., Villagrasa, P., et al. (2023). Assessment of the HER2DX Assay in Patients With ERBB2-Positive Breast Cancer Treated With Neoadjuvant Paclitaxel, Trastuzumab, and Pertuzumab. JAMA Oncol. *9*, 835–840. https://doi.org/10.1001/jamaoncol.2023.0181.
21. Braso-Maristany, F., Griguolo, G., Chic, N., Pascual, T., Pare, L., Maues, J., Galvan, P., Dieci, M.V., Miglietta, F., Giarratano, T., et al. (2023). HER2DX ERBB2 mRNA expression in advanced HER2-positive breast cancer treated with T-DM1. J Natl Cancer Inst *115*, 332–336. https://doi.org/10.1093/jnci/djac227.
22. Tarantino, P., Carmagnani Pestana, R., Corti, C., Modi, S., Bardia, A., Tolaney, S.M., Cortes, J., Soria, J.C., and Curigliano, G. (2022). Antibody-drug conjugates: Smart chemotherapy delivery across tumor histologies. CA Cancer J. Clin. *72*, 165–182. https://doi.org/10.3322/caac.21705.
23. Denkert, C., von Minckwitz, G., Darb-Esfahani, S., Lederer, B., Heppner, B.I., Weber, K.E., Budczies, J., Huober, J., Klauschen, F., Furlanetto, J., et al. (2018). Tumour-infiltrating lymphocytes and prognosis in different subtypes of breast cancer: a pooled analysis of 3771 patients treated with neoadjuvant therapy. Lancet Oncol. *19*, 40–50. https://doi.org/10.1016/s1470-2045(17)30904-x.
24. Lee, H.J., Kim, J.Y., Park, I.A., Song, I.H., Yu, J.H., Ahn, J.H., and Gong, G. (2015). Prognostic Significance of Tumor-Infiltrating Lymphocytes and the Tertiary Lymphoid Structures in HER2-Positive Breast Cancer Treated With Adjuvant Trastuzumab. Am. J. Clin. Pathol. *144*, 278–288. https://doi.org/10.1309/ajcpixuydvz0rz3g.
25. Massa, D., Vernieri, C., Nicolè, L., Criscitiello, C., Boissière-Michot, F., Guiu, S., Bobrie, A., Griguolo, G., Miglietta, F., Vingiani, A., et al. (2024). Immune and gene-expression profiling in estrogen receptor low and negative early breast cancer. J. Natl. Cancer Inst. *116*, 1914–1927. https://doi.org/10.1093/jnci/djae178.
26. Iwata, T.N., Ishii, C., Ishida, S., Ogitani, Y., Wada, T., and Agatsuma, T. (2018). A HER2-Targeting Antibody-Drug Conjugate, Trastuzumab Deruxtecan (DS-8201a), Enhances Antitumor Immunity in a Mouse Model. Mol. Cancer Ther. *17*, 1494–1503. https://doi.org/10.1158/1535-7163.Mct-17-0749.
27. Erber, R., and Hartmann, A. (2020). Histology of Luminal Breast Cancer. Breast Care *15*, 327–336. https://doi.org/10.1159/000509025.
28. Sima, C., and Dougherty, E.R. (2006). What should be expected from feature selection in small-sample settings. Bioinformatics *22*, 2430–2436. https://doi.org/10.1093/bioinformatics/btl407.
29. Ma, S., and Huang, J. (2008). Penalized feature selection and classification in bioinformatics. Brief. Bioinform. *9*, 392–403. https://doi.org/10.1093/bib/bbn027.
30. Bagherzadeh-Khiabani, F., Ramezankhani, A., Azizi, F., Hadaegh, F., Steyerberg, E.W., and Khalili, D. (2016). A tutorial on variable selection for clinical prediction models: feature selection methods in data mining could improve the results. J. Clin. Epidemiol. *71*, 76–85. https://doi.org/10.1016/j.jclinepi.2015.10.002.
31. Yu, G., Wang, L.G., Han, Y., and He, Q.Y. (2012). clusterProfiler: an R package for comparing biological themes among gene clusters. Omics *16*, 284–287. https://doi.org/10.1089/omi.2011.0118.
32. Love, M.I., Huber, W., and Anders, S. (2014). Moderated estimation of fold change and dispersion for RNA-seq data with DESeq2. Genome Biol. *15*, 550. https://doi.org/10.1186/s13059-014-0550-8.
33. Bankhead, P., Loughrey, M.B., Fernández, J.A., Dombrowski, Y., McArt, D.G., Dunne, P.D., McQuaid, S., Gray, R.T., Murray, L.J., Coleman, H.G., et al. (2017). QuPath: Open source software for digital pathology image analysis. Scientific reports *7*, 16878. https://doi.org/10.1038/s41598-017-17204-5.
34. Graham, S., Vu, Q.D., Raza, S.E.A., Azam, A., Tsang, Y.W., Kwak, J.T., and Rajpoot, N. (2019). Hover-Net: Simultaneous segmentation and classification of nuclei in multi-tissue histology images. Med. Image Anal. *58*, 101563. https://doi.org/10.1016/j.media.2019.101563.
35. Zhang, C., Xu, J., Tang, R., Yang, J., Wang, W., Yu, X., and Shi, S. (2023). Novel research and future prospects of artificial intelligence in cancer diagnosis and treatment. J. Hematol. Oncol. *16*, 114. https://doi.org/10.1186/s13045-023-01514-5.
36. Dai, M., Pei, X., and Wang, X.J. (2022). Accurate and fast cell marker gene identification with COSG. Brief. Bioinform. *23*, bbab579. https://doi.org/10.1093/bib/bbab579.
37. Dries, R., Zhu, Q., Dong, R., Eng, C.L., Li, H., Liu, K., Fu, Y., Zhao, T., Sarkar, A., Bao, F., et al. (2021). Giotto: a toolbox for integrative analysis and visualization of spatial expression data. Genome Biol. *22*, 78. https://doi.org/10.1186/s13059-021-02286-2.
38. Abkevich, V., Iliev, D., Timms, K.M., Tran, T., Skolnick, M., Lanchbury, J.S., and Gutin, A. (2010). Computational method for estimating DNA copy numbers in normal samples, cancer cell lines, and solid tumors using array comparative genomic hybridization. J Biomed Biotechnol *2010*. J. Biomed. Biotechnol. *2010*, 386870. https://doi.org/10.1155/2010/386870.

39. Lang, G.T., Jiang, Y.Z., Shi, J.X., Yang, F., Li, X.G., Pei, Y.C., Zhang, C.H., Ma, D., Xiao, Y., Hu, P.C., et al. (2020). Characterization of the genomic landscape and actionable mutations in Chinese breast cancers by clinical sequencing. Nat. Commun. *11*, 5679. https://doi.org/10.1038/s41467-020-19342-3.

40. Wang, K., Li, M., and Hakonarson, H. (2010). ANNOVAR: functional annotation of genetic variants from high-throughput sequencing data. Nucleic Acids Res. *38*, e164. https://doi.org/10.1093/nar/gkq603.

41. Talevich, E., Shain, A.H., Botton, T., and Bastian, B.C. (2016). CNVkit: Genome-Wide Copy Number Detection and Visualization from Targeted DNA Sequencing. PLoS Comput. Biol. *12*, e1004873. https://doi.org/10.1371/journal.pcbi.1004873.

42. Mermel, C.H., Schumacher, S.E., Hill, B., Meyerson, M.L., Beroukhim, R., and Getz, G. (2011). GISTIC2.0 facilitates sensitive and confident localization of the targets of focal somatic copy-number alteration in human cancers. Genome Biol. *12*, R41. https://doi.org/10.1186/gb-2011-12-4-r41.

43. Bergstrom, E.N., Kundu, M., Tbeileh, N., and Alexandrov, L.B. (2022). Examining clustered somatic mutations with SigProfilerClusters. Bioinformatics *38*, 3470–3473. https://doi.org/10.1093/bioinformatics/btac335.

44. Luebeck, J., Ng, A.W.T., Galipeau, P.C., Li, X., Sanchez, C.A., Katz-Summercorn, A.C., Kim, H., Jammula, S., He, Y., Lippman, S.M., et al. (2023). Extrachromosomal DNA in the cancerous transformation of Barrett's oesophagus. Nature *616*, 798–805. https://doi.org/10.1038/s41586-023-05937-5.

45. Chen, S. (2023). Ultrafast one-pass FASTQ data preprocessing, quality control, and deduplication using fastp. Imeta *2*, e107. https://doi.org/10.1002/imt2.107.

46. Kim, D., Paggi, J.M., Park, C., Bennett, C., and Salzberg, S.L. (2019). Graph-based genome alignment and genotyping with HISAT2 and HISAT-genotype. Nat. Biotechnol. *37*, 907–915. https://doi.org/10.1038/s41587-019-0201-4.

47. Pertea, M., Pertea, G.M., Antonescu, C.M., Chang, T.C., Mendell, J.T., and Salzberg, S.L. (2015). StringTie enables improved reconstruction of a transcriptome from RNA-seq reads. Nat. Biotechnol. *33*, 290–295. https://doi.org/10.1038/nbt.3122.

48. Johansson, T., Yohannes, D.A., Koskela, S., Partanen, J., and Saavalainen, P. (2021). HLA RNA Sequencing With Unique Molecular Identifiers Reveals High Allele-Specific Variability in mRNA Expression. Front. Immunol. *12*, 629059. https://doi.org/10.3389/fimmu.2021.629059.

49. Shui, Z., Zhang, S., Zhu, C., Wang, B., Chen, P., Zheng, S., and Yang, L. (2022). End-to-End Cell Recognition by Point Annotation (Springer Nature Switzerland)), pp. 109–118.

50. Wolff, A.C., Hammond, M.E.H., Allison, K.H., Harvey, B.E., Mangu, P.B., Bartlett, J.M.S., Bilous, M., Ellis, I.O., Fitzgibbons, P., Hanna, W., et al. (2018). Human Epidermal Growth Factor Receptor 2 Testing in Breast Cancer: American Society of Clinical Oncology/College of American Pathologists Clinical Practice Guideline Focused Update. J. Clin. Oncol. *36*, 2105–2122. https://doi.org/10.1200/JCO.2018.77.8738.

51. Farahmand, S., Fernandez, A.I., Ahmed, F.S., Rimm, D.L., Chuang, J.H., Reisenbichler, E., and Zarringhalam, K. (2022). HER2 and trastuzumab treatment response H&E slides with tumor ROI annotations. The Cancer Imaging Archive). https://doi.org/10.7937/E65C-AM96.

52. Aran, D., Hu, Z., and Butte, A.J. (2017). xCell: digitally portraying the tissue cellular heterogeneity landscape. Genome Biol. *18*, 220. https://doi.org/10.1186/s13059-017-1349-1.

53. Hu, C., Li, T., Xu, Y., Zhang, X., Li, F., Bai, J., Chen, J., Jiang, W., Yang, K., Ou, Q., et al. (2023). CellMarker 2.0: an updated database of manually curated cell markers in human/mouse and web tools based on scRNA-seq data. Nucleic Acids Res. *51*, D870–D876. https://doi.org/10.1093/nar/gkac947.

54. Sona, S., Bradley, M., and Ting, A.H. (2023). Protocols for single-cell RNA-seq and spatial gene expression integration and interactive visualization. STAR Protoc. *4*, 102047. https://doi.org/10.1016/j.xpro.2023.102047.

55. He, S., Bhatt, R., Brown, C., Brown, E.A., Buhr, D.L., Chantranuvatana, K., Danaher, P., Dunaway, D., Garrison, R.G., Geiss, G., et al. (2022). High-plex imaging of RNA and proteins at subcellular resolution in fixed tissue by spatial molecular imaging. Nat. Biotechnol. *40*, 1794–1806. https://doi.org/10.1038/s41587-022-01483-z.

56. Tan, C.L., Lindner, K., Boschert, T., Meng, Z., Rodriguez Ehrenfried, A., De Roia, A., Haltenhof, G., Faenza, A., Imperatore, F., Bunse, L., et al. (2025). Prediction of tumor-reactive T cell receptors from scRNA-seq data for personalized T cell therapy. Nat. Biotechnol. *43*, 134–142. https://doi.org/10.1038/s41587-024-02161-y.

57. Helzer, K.T., Sharifi, M.N., Sperger, J.M., Shi, Y., Annala, M., Bootsma, M.L., Reese, S.R., Taylor, A., Kaufmann, K.R., Krause, H.K., et al. (2023). Fragmentomic analysis of circulating tumor DNA-targeted cancer panels. Ann. Oncol. *34*, 813–825. https://doi.org/10.1016/j.annonc.2023.06.001.

58. Waljee, A.K., Weinheimer-Haus, E.M., Abubakar, A., Ngugi, A.K., Siwo, G.H., Kwakye, G., Singal, A.G., Rao, A., Saini, S.D., Read, A.J., et al. (2022). Artificial intelligence and machine learning for early detection and diagnosis of colorectal cancer in sub-Saharan Africa. Gut *71*, 1259–1265. https://doi.org/10.1136/gutjnl-2022-327211.

59. Qian, X., Pei, J., Zheng, H., Xie, X., Yan, L., Zhang, H., Han, C., Gao, X., Zhang, H., Zheng, W., et al. (2021). Prospective assessment of breast cancer risk from multimodal multiview ultrasound images via clinically applicable deep learning. Nat. Biomed. Eng. *5*, 522–532. https://doi.org/10.1038/s41551-021-00711-2.

60. Guerrero, C., Puig, N., Cedena, M.T., Goicoechea, I., Perez, C., Garcés, J.J., Botta, C., Calasanz, M.J., Gutierrez, N.C., Martin-Ramos, M.L., et al. (2022). A Machine Learning Model Based on Tumor and Immune Biomarkers to Predict Undetectable MRD and Survival Outcomes in Multiple Myeloma. Clin. Cancer Res. *28*, 2598–2609. https://doi.org/10.1158/1078-0432.Ccr-21-3430.

61. Collins, G.S., Dhiman, P., Ma, J., Schlussel, M.M., Archer, L., Van Calster, B., Harrell, F.E., Jr., Martin, G.P., Moons, K.G.M., van Smeden, M., et al. (2024). Evaluation of clinical prediction models (part 1): from development to external validation. Bmj *384*, e074819. https://doi.org/10.1136/bmj-2023-074819.

Please cite this article in press as: Ma et al., Spatial determinants of antibody-drug conjugate SHR-A1811 efficacy in neoadjuvant treatment for HER2-positive breast cancer, Cancer Cell (2025), https://doi.org/10.1016/j.ccell.2025.03.017

STAR★METHODS

KEY RESOURCES TABLE

REAGENT or RESOURCE	SOURCE	IDENTIFIER
Antibodies		
Anti-ER (SP1) Antibody	Ventana Roche	Cat#: 790-4325; RRID: AB_2335977
Anti-PR (1E2) Antibody	Ventana Roche	Cat#: 790-4296; RRID: AB_2335976
Anti-HER2/neu (4B5) Antibody	Ventana Roche	Cat#: 790-4493; RRID: AB_2921204
Anti-CD8α (C8/144B) Antibody	Cell Signaling Technology	Cat#: 70306; RRID: AB_2799781
Anti-CD8α Monoclonal antibody	Proteintech	Cat#: 66868-1-Ig; RRID: AB_2882205
Anti-CD68 Polyclonal Antibody	Proteintech	Cat#: 28058-1-AP; RRID: AB_2881049
Anti-PD-1/CD279 Polyclonal Antibody	Proteintech	Cat#: 18106-1-AP; RRID: AB_10732952
Anti-Granzyme B Polyclonal Antibody	Proteintech	Cat#: 13588-1-AP; RRID: AB_2114429
Anti-PDCD1LG2 Antibody	Sigma-Aldrich	Cat#: HPA013411; RRID: AB_1855102
Anti-Cytokeratin Antibody	Sigma-Aldrich	Cat#: C5992; RRID: AB_2134432
Critical commercial assays		
BenchMark ULTRA IHC/ISH System	Ventana Roche	RRID: SCR_025506
PathVysion HER2 DNA probe Kit	Vysis	Cat#: 02J01-035
Opal 6-Plex Manual Detection Kit	Akoya Biosciences	Cat#: NEL861001KT
Qubit 2.0 Fluorometer Qubit 2.0	Thermo Fisher Scientific	RRID: SCR_020553
Nanodrop Qubit 3.0 Fluorometer	Thermo Fisher Scientific	RRID: SCR_020311
DNBSEQ-T7 Genetic Sequencer	MGI	RRID: SCR_024847
TRIzol Reagent	Invitrogen	Cat#: 15596026
NovaSeq 6000 Sequencing System	Illumina	RRID: SCR_016387
Xenium Analyzer	10x Genomics	RRID: SCR_023910
Deposited data		
WGS, targeted and RNA sequencing, Xenium data	This study	National Genomics Data Center. BioProject ID: PRJCA036177
Xenium data	This study	The National Omics Data Encyclopedia, ID: OEP00006015
TCGA-BRCA H&E-stained WSIs	Cancer Imaging Archive	https://www.cancerimagingarchive.net/collection/her2-tumor-rois/
TCGA-BRCA RNA-seq	cBioPortal	https://www.cbioportal.org/
Software and algorithms		
BWA v0.7.17	Burrows–Wheeler Aligner	https://bio-bwa.sourceforge.net/
TNscope v202010.01	Sentieon	https://www.sentieon.com/
ANNOVAR v20200607	ANNOVAR	https://annovar.openbioinformatics.org/
CNVkit v0.9.9	Eric Talevich	https://cnvkit.readthedocs.io/
GISTIC_2.0	Broad Institute	https://broadinstitute.github.io/gistic2/
R v4.4.0	R	https://www.r-project.org/
R Studio	RStudio	https://www.rstudio.com/
Gene Set Enrichment Analysis (GSEA)	Broad Institute	http://software.broadinstitute.org/gsea/index.jsp
Python v3.12	Python	https://www.python.org/
PyCharm	JetBrains	https://www.jetbrains.com/pycharm/
clusterProfiler v4.12.0	Yu et al.[31]	https://github.com/YuLab-SMU/clusterProfiler
AmpliconSuite-pipeline v1.1.3	AmpliconSuite	https://github.com/AmpliconSuite/AmpliconSuite-pipeline
fastp v0.20.1	OpenGene	https://github.com/OpenGene/fastp
Hisat2 v2.1.0	DaehwanKimLab	https://github.com/DaehwanKimLab/hisat2

(*Continued on next page*)

Continued

REAGENT or RESOURCE	SOURCE	IDENTIFIER
Stringtie v2.2.1	The Center for Computational Biology at Johns Hopkins University	https://ccb.jhu.edu/software/stringtie/
DESeq2 v1.44.0	Love et al.[32]	https://bioconductor.org/packages/release/bioc/html/DESeq2.html
D-PathAI	Li et al.[18]	https://link.springer.com/chapter/10.1007/978-3-031-43987-2_52
QuPath v5.0.1	Bankhead et al.[33]	https://qupath.github.io/
HoVer-Net	Graham et al.[34]	https://github.com/vqdang/hover_net
sc-MTOP	Zhao et al.[11]	https://github.com/fuscc-deep-path/sc_MTOP
Seurat v5.1.0	Satija Lab	https://satijalab.org/seurat/
CellMarker_2.0	Zhang et al.[35]	http://bio-bigdata.hrbmu.edu.cn/CellMarker/index.html
COSG v0.9.0	Dai et al.[36]	https://github.com/genecell/COSG
Giotto v4.0.0	Dries et al.[37]	https://rubd.github.io/Giotto_site/index.html
scikit-learn v1.5.0	scikit-learn	https://scikit-learn.org/stable/index.html
SHAP v0.45.1	Su-In Lee's lab	https://pypi.org/project/shap/

EXPERIMENTAL MODEL AND STUDY PARTICIPANT DETAILS

Cohorts and study design

This study was approved and supervised by the Institutional Review Board of FUSCC. The full design of the FASCINATE-N trial is accessible at https://clinicaltrials.gov/ by ID NCT05582499. All enrolled patients were fully informed of their rights and signed written consent forms.

According to the Bayesian design of this clinical trial, for a certain treatment group, over the course of this study, efficacy was evaluated periodically at each additional 20 patients with completion of all the neoadjuvant therapy cycles and postsurgical efficacy assessments. Specifically, if the posterior probability of a treatment arm achieving a higher pCR rate than the conventional therapy was greater than 95%, the data of the primary, secondary efficacy endpoints and safety endpoints were combined to consider the graduation of the treatment group, and the graduation would not affect the enrollment of the corresponding cohort. In addition, if the posterior probability of a treatment arm achieving a higher pCR rate than the conventional therapy was less than 5%, the data of primary, secondary efficacy and safety endpoints were combined to consider the elimination of the precision therapy group, and the treatment plan of the precision therapy group would be updated. During the Bayesian monitoring of treatment efficacy, translational research was conducted to explore biomarkers that may guide more precise patient stratification. The findings of the translational research would be used to refine the adaptive design of the clinical trial. For the SHR-A1811 treatment group, the biomarker analysis was triggered upon the completion of all the first 60 patients.

For the efficacy prediction model, we used several cohorts for model training, testing, and external validation. The SHR-A1811 training cohort was derived from the 7:3 division of 60 SHR-A1811 patients and included 42 patients, with a pCR rate of 61.9%. The SHR-A1811 testing cohort, also from the same division, consisted of 18 patients, with a pCR rate of 66.7%, and was used to test the model's performance. For external validation, a real-world cohort was used, consisting of patients treated with neoadjuvant novel anti-HER2 ADC regimens in our center over the past 3 years. This cohort included 11 patients treated with T-DXd (pCR rate: 54.5%), 23 patients treated with SHR-A1811 (pCR rate: 60.9%), and 20 patients treated with TQB2102 (pCR rate: 65.0%). Additionally, the Neoadjuvant PCbHP cohort was derived from the standard PCbHP treatment arm of the HER2+ FASCINATE-N trial and used to examine whether our model could specifically predict the efficacy of novel ADCs as opposed to conventional dual-targeted therapies. This cohort included 60 patients, with a pCR rate of 68.3%.

Patient samples

Pretreatment tumor samples were obtained by Mammotome® Elite Tetherless Vacuum-Assisted Biopsy (Ohio, USA) or core needle biopsy. For patients biopsied at our center, after setting aside ample tissue for standard pathological assessment, the surplus tissue was fresh-frozen and stored in liquid nitrogen. Basically, for these fresh frozen samples, the limited tissue amount dictated the order of multiomic testing: targeted sequencing > RNA-seq > WGS. For patients having biopsies performed at other hospitals, their pathological results were re-validated at our center through independent staining and evaluation on formalin-fixed paraffin-embedded (FFPE) sections. And molecular profiling was not conducted due to lack of fresh-frozen samples. Apart from one RNA-sequencing sample excluded due to insufficient RNA quantity (less than 100 ng required for library preparation), no other samples were excluded based on quality criteria.

Pretreatment peripheral blood was centrifuged, and red blood cells were lysed to obtain peripheral blood mononuclear cells (PBMCs). PBMCs were resuspended in cell cryopreservation solution and stored at -80°C.

Please cite this article in press as: Ma et al., Spatial determinants of antibody-drug conjugate SHR-A1811 efficacy in neoadjuvant treatment for HER2-positive breast cancer, Cancer Cell (2025), https://doi.org/10.1016/j.ccell.2025.03.017

METHOD DETAILS

Pathological tests

Immunohistochemistry (IHC) was performed by the central laboratory in the Department of Pathology of FUSCC. Pathology results were confirmed independently by two experienced pathologists. A Ventana BenchMark Ultra Automated Stainer (Ventana Roche, Tucson, Arizona, USA) and a Ventana Ultra View universal DAB detection kit (Ventana Roche, Tucson, Arizona, USA) were used to perform IHC staining. ER/PR positivity was defined as $\geq$1% positively stained invasive cancer cells. The final HER2 status was determined according to the latest American Society of Clinical Oncology/College of American Pathologists (ASCO/CAP) guidelines. Tumor-infiltrating lymphocytes (TILs) were evaluated on H&E-stained slides by two experienced pathologists independently following the guidelines provided by the International TILs Working Group.[38] IHC staining was performed with Ventana ER (SP1), PR (IE2) and HER2 (4B5). Dual-probe fluorescence *in situ* hybridization (FISH) was performed using the PathVysion HER2 DNA probe Kit (Vysis Inc., Downers Grove, IL). Evaluation was conducted on baseline core biopsy samples. The percentage of stromal TILs (defined as the proportion of stromal area occupied by mononuclear immune cells relative to the total stromal area within the region of interest) was quantified visually for each sample. The scoring was performed on a continuous scale in 5% increments. When discrepancies between pathologists did not exceed 10%, the mean value was adopted. Otherwise, a third qualified pathologist was involved to conduct a joint review.

Multiplex immunofluorescence assay

A 6-plex immunofluorescence (IF) assay was performed using the Opal Polaris 6 Color Manual IHC Detection Kit (Akoya Biosciences, NEL861001KT) to detect CD8, PDCD1, GZMB, PDCD1LG2, panCK, and DAPI. The anti-CD8 antibody (1:10000; mouse mAb; Proteintech; Cat# 66868-1-Ig, RRID: AB_2882205) was labeled with the Opal Polaris 690 (1:100). Similarly, the anti-PD1 antibody (1:1000; rabbit mAb; Proteintech; Cat# 18106-1-AP, RRID: AB_10732952) was labeled with the Opal Polaris 480 (1:100). The anti-GZMB antibody (1:100; rabbit mAb; Proteintech; Cat# 13588-1-AP, RRID: AB_2114429) was labeled with the Opal Polaris 570 (1:100). The anti-PDL2 antibody (1:100; rabbit mAb; Sigma-Aldrich; Cat# HPA013411, RRID: AB_1855102) was labeled with the Opal Polaris 520(1:100). The anti-Cytokeratin antibody (1:200; mouse mAb; Sigma-Aldrich; Cat# C5992, RRID: AB_2134432) was labeled with the Opal Polaris 780 (1:25).

All slides were scanned using the Vectra Polaris (Perkin Elmer). QuPath (version 0.5.1) was used for image stitching, tissue annotation, cell detection, cell phenotyping, pixel classification. Cytotoxic T cells were indicated by CD8 and GZMB, and tumors cells were indicated by panCK.

Targeted sequencing

Tumor samples were sequenced using the FUSCC-BC panel (539-gene) as previously described.[39] Basically, the panel targets mutations, small insertions/deletions, and copy number alterations that frequently impact breast cancer.

Whole-genome sequencing (WGS)

DNA extraction

For fresh frozen tissue total DNA was extracted from the 10 mg tissues using QIAamp DNA Mini Kit (Qiagen-51306) according to the manufacturer's instructions. For paired peripheral blood mononuclear cell: Total DNA was extracted from the1 mL blood using QIAamp DNA Blood Mini Kit (Qiagen-51106) according to the manufacturer's instructions. Then the integrity and concentration of the total DNA was determined by agarose electrophoresis and Qubit 2.0 fluorometer dsDNA HS Assay (Thermo Fisher Scientific). OD260/OD280 was measured by NanoDrop2000 (Thermo Fisher Scientific).

Library preparation

About 50 ng of high-quality genomic DNA was sheared with Covaris LE220 Sonicator (Covaris) to about 350 bp. The library was constructed according to the protocol of the KAPA Hyper Prep kit (Roche). First the fragmented DNA was purified using sample purification beads, and the product was repaired by the end and A base was added to the 3 'end. Then, the adapters are ligated with the specific barcode sequence. The CleanNGS magnetic beads (CleanNA) were used to screen out incomplete connections and self-connecting products. Sequencing libraries were formed by PCR amplification using universal primers complementary to the adaptor sequences.

Library quality control

After library construction, the Qubit 3.0 fluorometer dsDNA HS Assay (Thermo Fisher Scientific) was used to quantify the concentration of the libraries, while the size distribution was analyzed by Agilent Bioanalyzer 4200 (Agilent).

Sequencing

Paired-end sequencing was performed using the MGI DNBSEQ-T7 RS FCL DNA library prep set V3.0 (PE150) on the MGI DNBSEQ-T7 platform (MGI, Shenzhen, China) by Sequanta technologies (Shanghai, China) according to the manufacturer's instructions.

Somatic mutation calling

Raw Sequence data were first aligned to the human reference genome GRCh38 (https://gdc.cancer.gov/about-data/gdc-data-processing/gdc-reference-files) using Burrows–Wheeler Aligner (BWA version 0.7.17) with default parameters. For each paired sample, somatic SNVs and InDels were detected by Sentieon TNscope (version 202010.01). Furthermore, in order to filter out germline variants, we generated a generic panel of normal (PON) file using the matched normal samples. Mutations in low complexity regions

such as tandem repeat regions and highly homologous regions in the genome were filtered out. Low confidence variants were removed if any one of the following criteria was not satisfied: alternative allele depth in tumor >=3, variant allele frequency in tumor >= 0.05 (if a mutation is annotated as a cosmic database somatic mutation, alternative allele depth in tumor >=2, variant allele frequency in tumor >= 0.03), variant allele frequency in normal / variant allele frequency in tumor < 0.2. Finally, all high-confident mutations were then annotated with ANNOVAR (version 20200607).[40]

Copy number alteration calling and profiling

We used CNVkit (version 0.9.9) software to detect somatic copy number alterations (SCNAs) on the genome.[41] We used a 5 kb bin size to analyze the whole-gene copy number variation. First, calculate the cnn (copy number coverage) information for each bin size of the sample. Secondly, comparing the cnn file with the reference sequence and simultaneously correcting the bias and GC content, a copy number ratio (cnr) file of the sample is obtained. Again, we use the CBS (Circular binary segmentation) algorithm to connect the cnr file with a similar log2 value to the bin size to obtain information about the change in the number of copies of the segment region. To further analyze the gene-level CNAs, we employed GISTIC 2.0 (Genomic Identification of Significant Targets in Cancer).[42] Both gene-level and broad-level analyses were performed to ensure comprehensive detection of significant regions. A q-value threshold of 0.05 was applied to control the false discovery rate, and a confidence level of 0.95 was set for determining the significance of regions. Broad regions were considered significant if they covered at least 98% of the chromosome arm length. Additionally, the log2 ratio of copy numbers was capped at 3.5 to prevent outliers from distorting the results, and the maximum number of segments allowed in the input file was set to 15,000, accommodating large datasets and ensuring comprehensive analysis. Gene-level results were saved for detailed examination, providing insights into potential genomic drivers of cancer.

Other genomic events calling

Somatic mutations were used as input of SigProfilerClusters[43] (version 1.1.2) to identify the kataegis. The kataegis burden was defined as the number of mutations classified as kataegis. AmpliconSuite-pipeline (version 1.1.3) was used to detect amplicons.[44]

RNA-sequencing

RNA extraction

Total RNA was extracted from the 10 mg tissues after grinding by Homogenizer (Scientz) using TRIzol® Reagent (Invitrogen) and RNeasy minElute spin column (Qiagen) according to the manufacturer's instructions. Then the integrity of the total RNA was determined by 2100 Bioanalyser (Agilent) and quantified using the NanoDrop (Thermo Scientific). About 500 ng high-quality RNA sample (OD260/280=1.9∼2.0, RIN≥3) was used to construct the sequencing library.

Library preparation

RNA purification, reverse transcription, library construction and sequencing were performed at Sequanta Technologies in Shanghai according to the manufacturer's instructions. The rRNA and globin mRNA-depleted sequencing libraries from 100ng total RNA were prepared using Stranded Total RNA preparation, Ligation with Ribo-Zero Plus kit (Illumina). Both cytoplasmic, mitochondrial rRNA and globin mRNA were depleted from total RNA. After purification of the remaining RNA without rRNA and globin mRNA, the RNA was fragmented into small pieces using divalent cations under elevated temperature. The cleaved RNA fragments are copied into first strand cDNA using reverse transcriptase and random primers. Then in the process of second strand cDNA synthesis, the RNA template was removed and a replacement strand, incorporating dUTP in place of dTTP to generate ds cDNA, was synthesized. The incorporation of dUTP quenches the second strand during amplification, because the polymerase does not incorporate past this nucleotide. AMPure XP (Beckmen) beads were then used to purify the ds cDNA from the reaction mix. These ds cDNA fragments were then subjected to end-repair, phosphorylation and 'A' base addition according to Illumina's library construction protocol. The products were purified and enriched with PCR, and the AMPure XP Beads (Beckmen) were used to clean up the amplified target fragments of 200–300 bp to create the final library.

Sequencing

After library construction, the Qubit 3.0 fluorometer dsDNA HS Assay (Thermo Fisher Scientific) was used to quantify the concentration of the resulting sequencing libraries, while the size distribution was analyzed using Agilent BioAnalyzer (Agilent). Sequencing was performed using an Illumina Novaseq 6000 following Illumina-provided protocols for 2x150 paired-end sequencing in Sequanta Technologies Co., Ltd (Shanghai, China).

RNA-seq analysis

Raw reads were trimmed with fastp (version 0.20.1) to remove adapter sequences and the reads whose length were longer than 75bp were selected after adapters were removed.[45] Then the selected reads, named as clean reads, were aligned to the human reference genome GRCh38 (https://benlangmead.github.io/aws-indexes/hisat) with Hisat2 (version 2.1.0).[46] Gene expression abundance was estimated by Strintie (version 2.2.1) based on the uniquely mapped reads.[47]

Bioinformatic analyses

Differentially expressed genes (DEGs) were identified using the R package "DESeq2" (version 1.44.0) according to official instructions.[32] HLA genes were excluded because of the inaccuracy of identifying highly polymorphic and homologous HLA alleles from short-read RNA-seq.[48] Enrichment analysis based on DEGs was performed using the R package clusterProfiler (version 4.12.0).[45] For enrichment analysis, gene sets belonging to HALLMARK, GOBP, REACTIOME and KEGG categories were included, which were downloaded from https://www.gsea-msigdb.org/gsea/msigdb/index.jsp.

Please cite this article in press as: Ma et al., Spatial determinants of antibody-drug conjugate SHR-A1811 efficacy in neoadjuvant treatment for HER2-positive breast cancer, Cancer Cell (2025), https://doi.org/10.1016/j.ccell.2025.03.017

Digital pathology

Segmentation and classification of tumor and TME cells

In our current research, we aimed to differentiate various tumor cell types based on the membrane expression status and intensity of HER2. Additionally, we sought to identify the tumor microenvironment (TME) components surrounding these cells. To achieve this goal, we employed two distinct methodologies for the segmentation, classification, and localization of cellular compartments using paired Her2 IHC-stained WSIs and H&E-stained WSIs.

For distinct types of breast cancer cells, we utilized the D-PathAI platform, an innovative deep learning framework for membrane segmentation that leverages nuclei point-level supervision from HER2 IHC images.[13,49] This framework comprises two networks: Seg-Net, which generates segmentation results for the membranes and nuclei of various tumor cells with different HER2 expression statuses, and Tran-Net, which transforms these segmentations into semantic points. Seg-Net uses a U-Net architecture with residual connections to enhance feature extraction and segmentation accuracy. It is trained with a custom loss function that combines binary cross-entropy and dice coefficient to address class imbalance. Tran-Net, based on a transformer model, encodes segmented images into semantic points, capturing essential spatial relationships and contextual information for accurate cell type discrimination. This approach allowed us to accurately identify and position breast tumor cells with three types of HER2 expression statuses on the cell membrane: negative HER2 expression, weak HER2 expression (including incomplete membrane staining that is faint or barely perceptible, as well as weak to moderate complete membrane staining, corresponding negative (1+) and equivocal (2+) HER2 IHC status), and strong HER2 expression (HER2 staining that is complete and intense, corresponding positive (3+) HER2 IHC status), according to the 2018 ASCO-CAP recommendations for HER2 testing.[50] For each HER2 IHC WSI, D-PathAI provided the coordinates of the three types of breast tumor cells and nontumor cellular components.

For the microenvironment cells, we applied Hover-Net for nuclear segmentation and cell type classification based on H&E-stained WSIs.[34] This network utilizes a dual-branch architecture to perform nuclear instance segmentation and classification. The segmentation branch uses a fully convolutional network (FCN) to generate detailed nuclear boundaries, while the classification branch employs a convolutional neural network (CNN) to assign class labels to each segmented nucleus. This design allows Hover-Net to identify five nuclear types, including immune, stromal, cancer, normal epithelial, and necrotic cells. The network is trained on a large dataset of annotated H&E-stained images using a multitask loss function that balances segmentation accuracy and classification performance. In this study, we specifically focused on immune cells and stromal cells, the primary functional players in the tumor microenvironment. We detected and extracted the nuclear types corresponding to immune, stromal, and tumor cells and classified them into three main types. This information was then used for subsequent topological analysis. To evaluate the reliability of TME features derived from H&E-stained WSIs, we collected HER2+ tumors with paired H&E-stained WSIs and RNA-seq from the TCGA-BRCA cohort (N=104)[51] and the CBCGA cohort (N=151).[15] The abundance of immune cells was inferred by xCell deconvolution algorithm.[52] Then Spearman's correlation analysis was performed to evaluate the correlation between TME features derived from H&E-stained WSIs and xCell.

Cellular interactions revelation of topological features

To comprehensively profile the interactions between various HER2 expression breast cancer cells and their interplay with microenvironmental compartments, we extracted topological features to characterize the intercellular relationships at single-cell resolution using the single-cell morphological and topological profiling (sc-MTOP) framework. This graph-based framework constructs a graph for each pair of cell types. Ultimately, seven graphs were constructed, including HER2_strong-HER2_strong, HER2_strong-HER2_weak, HER2_strong-HER2_neg, and HER2_weak-HER2_neg for IHC WSIs and tumor-immune, tumor-stromal, and immune-immune for H&E-stained WSIs. For each cell pair within the graphs, a k-nearest neighbor algorithm was used for edge configuration based on the hypothesis that spatially proximal cells are more likely to interact. This algorithm computes distances in a high-dimensional feature space, efficiently determining the nearest neighbors for each cell. Further filtering and removal of redundant edges were performed using a 25 μm threshold, determined through empirical analysis to balance sensitivity and specificity in interaction detection.

After constructing these multilevel pairwise graphs, we computed the topological features for each graph and concatenated them to form comprehensive topological profiles. For each graph type, topological features included the following: i) edge length-related features, MinEdgeLength and MeanEdgeLength, representing the minimum and average edge lengths of a cell, respectively; ii) Nsubgraph, the cell number within the subgraph where the cell is located; and iii) degrees, the number of edges connecting the cell to surrounding cells of the interacting cell types. Additionally, advanced graph metrics such as the clustering coefficient and betweenness centrality were calculated to provide deeper insights into the structural properties of the cellular network. Furthermore, the sc-MTOP pipeline was employed to identify topological features in cellular interactions between cancer cells and microenvironment components, as identified by the Xenium *in situ* platform. Detailed information on the sc-MTOP algorithm is available in our referenced publication.

Independent cohort to study the relation of HER2 distribution and molecular features

We scanned archived HER2-IHC-stained slides from patients in the CBCGA cohort who underwent RNA-seq profiling. This process resulted in a dataset comprising 55 paired HER2-IHC slides and corresponding RNA-seq profiles.

Xenium profiling

For each patient, the region of interest was dissected from a 5-μm formalin-fixed paraffin-embedded tissue film. A 380-gene panel (a predesigned 280-gene panel for breast cancer and a 100-gene custom panel) was used. The profiling process and cell segmentation were carried out according to the manufacturer's instructions (10x Genomics, CA, USA) by Precision Medicine Technologies Co., Ltd. (Shanghai, China).

Please cite this article in press as: Ma et al., Spatial determinants of antibody-drug conjugate SHR-A1811 efficacy in neoadjuvant treatment for HER2-positive breast cancer, Cancer Cell (2025), https://doi.org/10.1016/j.ccell.2025.03.017

Xenium analysis

Data loading and cell type identification

Xenium data were loaded into R by Seurat (v5.1.0) according to the Seurat vignette. The loaded data were subjected to transform-based normalization (*SCTransform*), followed by PCA dimensionality reduction (*RunPCA*) and layer integration (*IntegrateLayers*). *FindNeighbors* and *FindClusters* were used to find cell subclusters at the optimal resolution. Major cell types (cancer cells, adipocytes, B cells, breast glandular cells, dendritic cells, endothelial cells, fibroblasts, macrophages, mast cells, myoepithelial cells, perivascular cells, and T cells) were first identified, and cell subtypes were subsequently identified within certain cell types. Annotations were aided by cell markers according to CellMarker 2.0 (http://bio-bigdata.hrbmu.edu.cn/CellMarker/index.html).[53] Differential expression analyses between cell groups were carried out by COSG (version 0.9.0).[36]

Spatial cell-level ligand–receptor interaction pairs

Spatial networks were built using the Giotto package[54] (https://rubd.github.io/Giotto_site/index.html) to connect single cells based on their physical distance. Using the Delaunay method, neighbors are determined via Delaunay triangulation and a maximum distance criterion. After that, L-R (ligand–receptor) interactions were scored using the Delaunay network built above. The desired linkages were extracted from the network and used to calculate the L-R interaction score, which measures pairwise L-R expression between specified cell types. Linkages are reoriented to differentiate between ligand- and receptor-expressing cells. This score is compared with a distribution of scores produced using randomized linkages to determine whether the given configuration of interactions between specified cell types significantly enriches for pairwise L-R expression.

Spatial niche

We created a neighborhood matrix using the number of each cell type among each cell's 200 closest neighbors using the cell center coordinate information in 2D physical space.[55] After integrating the neighborhood matrix. Five percent of the cells of each tissue were sampled, and an AnnData object was generated using the integrated sampled matrix. Then, to define niches, Leiden clustering was performed on this integrated AnnData object, while the remaining cell types were identified using the ingest function in the Scanpy package in Python. Niches that consisted of less than five percent of all detected cells were discarded.

Model construction for efficacy prediction

Cohorts for modeling

The SHR-A1811 cohort was firstly split to form a SHR-A1811 training cohort (n = 42) and a SHR-A1811 testing cohort (n = 18). A 7:3 ration was adopted, which was a widely used ratio for dividing training and testing cohorts, as summarized by Zhang et al.[35] and used by many other studies.[56–60] A real-world neoadjuvant ADC validation cohort for model validation and a neoadjuvant PCbHP cohort for testing the specifity of the model were also included. Detailed description of these cohorts is provided under the cohorts and study design section and Tables S8 and S9.

Multidimensional data inclusion and selection

To address the small sample size, we employed feature selection not only to reduce dimensionality but also to minimize the risk of overfitting. For clinicopathological variables, we included the 8th edition of the AJCC staging system and HR status. For digital pathology, we incorporated all digital pathology variables, including cellular proportion features and cellular topology interaction features, such as edge features, subgraph features, and node features, totaling 38 digital pathology variables. Categorical variables were encoded separately. In the variable selection phase, we first eliminated collinear variables with a collinearity index greater than 0.8. Then, we performed a Mann–Whitney U test for all variables against therapeutic efficacy, removing variables with weak correlations. This process allowed us to retain 13 robust predictive variables (Figure S6A), facilitating the development of a reliable efficacy prediction model and elucidating the differential mechanisms of various anti-HER2 targeted therapies. Among these variables, clinical and pathological variables included American Joint Committee on Cancer (AJCC) stage. The cellular proportion characteristics included the proportion of immune cells and the proportion of HER2-expressing cells among all cells. Edge features comprised five variables: HER2strong_HER2strong_minEdgeLength, HER2weak_HER2null_minEdgeLength, HER2strong_HER2weak_minEdgeLength, Immune_Immune_minEdgeLength, and Tumor_Immune_minEdgeLength. Subgraph features included four variables: HER2strong_HER2strong_Nsubgraph, HER2strong_HER2null_Nsubgraph, HER2weak_HER2null_Nsubgraph, and Immune_Immune_Nsubgraph. Additionally, a node feature was considered: HER2strong_HER2null_Degrees.

Multimodel integration

Following feature selection, we standardized the data for modeling. The data standardization process involved scaling features to zero mean and unit variance using StandardScaler from scikit-learn to ensure that all variables contributed equally to the model. Given the relatively small number of patients and variables in this study, we utilized Python (version 3.12), numpy (version 2.0.0), and pandas (version 2.2.2), employing the scikit-learn (version 1.5.0) library for logistic regression, K-nearest neighbors (KNN), Gaussian naive Bayes, and Bernoulli naive Bayes models.

We optimized all the hyperparameters through a grid search using 10-fold cross-validation. The models' performance was evaluated using the area under the curve (AUC) of the receiver operating characteristic (ROC) curve, a robust metric for binary classification tasks. To measure the reliability of the model, we calculated the confidence intervals (CIs) for the area under the curve (AUC). For each model trained with a unique random seed, we used the bootstrap method with 200 resamples. To mitigate biases and overfitting associated with individual models, we employed the ensemble learning technique through a voting classifier from sklearn.ensemble. This method combined the predictions from all four models by averaging their predicted probabilities (soft voting) to form a more robust and generalizable predictive model. Using the final voting model, we applied SHapley Additive ExPlanations (SHAP)

0.45.1 for model interpretability scoring. SHAP values helped us quantify the contribution of each feature to the model's predictions, thereby offering insights into the importance of various clinical and digital pathology variables in determining therapeutic efficacy.

Finally, we validated the model using the SHR-A1811 testing cohort and the real-world ADC cohort. To assess the stability and robustness of our model's performance, we repeated the training and validation process using 500 different random seeds. For each of these models, we applied the bootstrap method as described. This combined approach ensured that our results were not dependent on a specific data sample or random initialization, thereby enhancing the credibility and reproducibility of our findings.[61]

QUANTIFICATION AND STATISTICAL ANALYSIS

Comparisons of ordered class variables and continuous variables were performed by the Kruskal–Wallis rank sum test. Comparisons of categorical variables were performed by Fisher's exact test or the chi-square test, where appropriate. False discovery rates (FDRs) were obtained using the p.adjust function in R with the "fdr" method. All analyses above were performed in R version 4.4.0.